Wei et al. *Zool. Res.* 2026, 47(2): 503−518
https://doi.org/10.24272/j.issn.2095-8137.2025.220
https://cstr.cn/32248.14.zr.2025.220

ZR | Zoological Research

Article Open Access

Male germ cell-specific deletion of *Eif5* causes the apoptosis of mouse progenitor spermatogonia by excessive endoplasmic reticulum stress and defective DNA repair

Hongwei Wei[1], Yating Huang[1], Weiyong Wang[1], Shuang Liu[1], Huiyu Liu[1], Hanyu Chu[1], Yan-Li Sun[1], Yan Du[1], Wenqian Li[1], Luchun Zhang[1], Yashuang Weng[1], Wenbo Zhang[1], Meijia Zhang[1,*], Zhijuan Wang[2,*]

[1] *The Innovation Centre of Ministry of Education for Development and Diseases*, *School of Medicine*, *South China University of Technology*, *Guangzhou*, *Guangdong* 510006, *China*

[2] *Affiliated Zhuhai Women and Children's Hospital*, *South China University of Technology (Zhuhai Center for Maternal and Child Health Care)*, *Zhuhai*, *Guangdong* 519001, *China*

ABSTRACT

Idiopathic non-obstructive azoospermia (iNOA) is associated with reduced expression of multiple eukaryotic translation initiation factors (*EIFs*) in spermatogonia, including eukaryotic translation initiation factor 5 (*EIF5*). The present study revealed that eIF5 mRNA and protein levels were markedly higher in male mouse (*Mus musculus*) germ cells than in Leydig or Sertoli cells. Thus, to define the role of eIF5 in spermatogenesis, *Eif5* conditional knockout (cKO) mice were generated by crossing *Eif5*$^{fl/fl}$ mice with *Stimulated by retinoic acid 8* (*Stra8*)-Cre mice. Loss of *Eif5* in male germ cells reduced both SRY-box transcription factor 3 (SOX3)$^{+}$ progenitor spermatogonia and Kit proto-oncogene receptor tyrosine kinase (KIT)$^{+}$ differentiating spermatogonia, leading to severe meiotic failure and complete male infertility. Mechanistically, *Eif5* deficiency impaired translation of genes involved in ubiquitination, autophagy, and DNA repair, which, in turn, triggered excessive endoplasmic reticulum (ER) stress and compromised DNA repair in SOX3^{+} progenitor spermatogonia. These defects promoted DNA damage and subsequent apoptosis, resulting in progressive germ cell depletion and sterility. Collectively, these findings highlight the essential role of eIF5 in spermatogenesis and offer a potential therapeutic strategy for iNOA associated with reduced expression of *EIF5* and other translation initiation factors.

Keywords: eIF5; Endoplasmic reticulum stress; DNA repair; Male infertility

INTRODUCTION

Spermatogenesis is a highly coordinated and tightly regulated developmental program that persists throughout the male lifespan (Ki et al., 2022). Within seminiferous tubules, spermatogonial stem cells (SSCs) undergo self-renewal through mitotic division to sustain the stem cell pool or commit to differentiation, giving rise to progenitor spermatogonia (Liu et al., 2022; Wang et al., 2019). These progenitor cells subsequently transition into differentiating spermatogonia and further differentiate into preleptotene spermatocytes (Liu et al., 2022; Lu et al., 2022; Xu et al., 2021). Entry into meiosis initiates a complex series of chromosomal events that ultimately generate haploid spermatids, which then undergo extensive morphological remodeling to form elongated spermatozoa characterized by specialized flagellar structures (Huang et al., 2021; Li et al., 2022c; Yin et al., 2021).

Protein translation is precisely regulated throughout spermatogenesis. During the mitotic phase, proliferation and lineage commitment of spermatogonia depend on robust protein synthesis to support DNA replication, genome maintenance, cell cycle progression, and survival, including production of DNA repair factors, ubiquitination-related proteins, and cell cycle regulators (Li et al., 2023; Qin et al., 2022; Wang et al., 2017). During meiosis, successful generation of haploid round spermatids requires translation of meiosis-specific factors involved in synaptonemal complex assembly, homologous recombination, and chromatin segregation (Anderson et al., 2019; Da Ines et al., 2022). During spermiogenesis, the transformation of round spermatids into highly specialized spermatozoa is accompanied by large-scale structural reorganization that

Received: 22 September 2025; Accepted: 18 November 2025; Online: 19 November 2025

Foundation items: This work was supported by the National Key Research and Development Program of China (2022YFC2703000 to M.Z.), National Natural Science Foundation of China (U24A20662 and 32270900 to M.Z.; 32500743 to Z.W.), and Guangdong Basic and Applied Basic Research Foundation (2023A1515220062 to Z.W.)

*Corresponding authors, E-mail: zhangmeijia@scut.edu.cn; zhijuanwang215@gmail.com

demands elevated translational output, including synthesis of protamines and components of the fibrous sheath (Vedanayagam et al., 2021; Zhang et al., 2022d). Thus, precise spatiotemporal regulation of protein translation is essential for coordinated progression of spermatogonial proliferation and differentiation.

Eukaryotic translation initiation is governed by a coordinated network of regulatory factors. Formation of the ternary complex, consisting of eukaryotic translation initiation factor 2 (eIF2), guanosine triphosphate (GTP), and initiator methionyl transfer RNA (Met-tRNAi), drives assembly of the 43S pre-initiation complex (PIC) together with the 40S ribosomal subunit and associated factors eIF1, eIF1A, and eIF3 (Li et al., 2022b; Shu et al., 2022; Young-Baird et al., 2019). Recruitment of the 43S PIC to mRNA and accurate start codon recognition are facilitated by the eIF4F complex, followed by binding to the 60S ribosomal subunit for translation initiation (Berzal-Herranz et al., 2022; Eliseev et al., 2018; Yang et al., 2017). Upon start codon recognition, eIF5 stimulates GTP hydrolysis on eIF2, generating inactive eIF2·GDP and promoting its release from the ribosome (Li et al., 2022b; Singh et al., 2021). Reactivation of eIF2 is subsequently mediated by eIF2B which catalyzes exchange of GDP for GTP to enable successive rounds of translation initiation (Young-Baird et al., 2020). Perturbation of eIF5 function has been linked to reproductive impairment across multiple systems. In *Drosophila* testes, *eIF5* knockdown in cyst stem cells disrupts germ cell differentiation and results in infertility (Li et al., 2022b). In mice, *Eif5* deletion induces oocyte apoptosis through mitochondrial fission defects and accumulation of DNA damage (Wang et al., 2024), whereas *Eif5* overexpression in zygotes inhibits embryonic development by enhancing global non-AUG translation (Zhang et al., 2022c). A recent transcriptomic analysis shows that dysregulation of *EIF* family members is detected in the spermatogonia of 13 iNOA, in which *EIF5* expression is downregulated in 7 patients and upregulated in 6 patients. (Chen et al., 2023). In these cases, spermatogenic progression is arrested at the spermatocyte stage, and mature sperm are absent from epididymal samples. Despite these observations, the causal relationship between eIF5 dysfunction and spermatogenic failure remains unclear.

In the present study, *Eif5* was conditionally ablated in male germ cells to define its functional role during spermatogenesis. Notably, loss of *Eif5* induced DNA repair defects and endoplasmic reticulum (ER) stress, which promoted apoptosis of $SOX3^+$ progenitor spermatogonia.

MATERIALS AND METHODS

Animals

Eif5$^{flox/flox}$ mice were obtained from the Shanghai Model Organisms Center, Inc. (China) (Wang et al., 2024). To generate germ cell-specific conditional knockout (cKO) models, *Eif5*$^{flox/flox}$ mice were crossed with *Stimulated by retinoic acid 8* (*Stra8*)-Cre mice (Lu et al., 2022). Genomic DNA extracted from mouse tissue was used for genotyping by polymerase chain reaction (PCR). Primer sequences used for identification of *Eif5*$^{flox/flox}$ and *Stra8*-Cre mice are provided in Supplementary Table S1. All experimental procedures involving animals were approved by the Institutional Animal Care and Use Committee of the South China University of Technology (Approval No.: 2024084).

Leydig cell isolation

Leydig cells were isolated from the testes of 3-week-old mice using a modified protocol based on a previously described method (Yuan et al., 2021). Briefly, testicular tissue was digested using collagenase II (C6885; Sigma-Aldrich, Germany), followed by filtration to obtain a single-cell suspension. Cells were then subjected to density gradient centrifugation using a Percoll gradient composed of 60%, 37%, 26%, and 21% concentrations (BS909, Biosharp, China). Centrifugation was performed at 2 500 ×*g* for 25 min at 4℃. Cells located at the interphase between the 60% and 37% Percoll layers were collected and identified by 3β-hydroxysteroid dehydrogenase (3β-HSD) staining.

Sertoli cell isolation

Sertoli cells were isolated from the testes of 3-week-old mice using a modified protocol adapted from a previously established method (Saewu et al., 2020). After removal of the tunica albuginea, testes were washed three times with phosphate-buffered saline (PBS) and sequentially subjected to enzymatic digestion using three solutions. Digestive solution 1 contained 0.1% (w/v) collagenase IV (C5138, Sigma-Aldrich, USA) and 0.01% (w/v) DNase Ⅰ (10104159001, Roche, Switzerland) in Dulbecco's Modified Eagle Medium/Nutrient Mixture F-12 (DMEM/F12). Digestive solution 2 contained 0.1% collagenase IV, 0.1% (w/v) hyaluronidase (H3506, Sigma-Aldrich, USA), and 0.01% DNase I in DMEM/F12. Digestive solution 3 contained 0.1% collagenase, 0.1% hyaluronidase, 0.25% (w/v) trypsin (EDTA-free) (T1426, Sigma-Aldrich, USA), and 0.01% DNase I in DMEM/F12. After digestion, the cell suspension was filtered through a 40 μm filter (BD Falcon, USA). Cells were cultured at 37°C in an incubator with 5% CO_2. After 48 h, residual germ cells were removed by brief treatment with 20 mmol/L Tris (pH 7.4) for 2–3 s. Cell identity was confirmed by staining for SRY-box transcription factor 9 (SOX9).

Germ cell isolation

Undifferentiated spermatogonia marked by Thy-1 cell surface antigen (THY1) and differentiating spermatogonia marked by KIT were isolated using magnetic-activated cell sorting (MACS; Miltenyi, Germany) in accordance with the manufacturer's protocols. Spermatocytes were obtained by bovine serum albumin (BSA) gradient sedimentation, as described previously (Ki et al., 2022; Li et al., 2022c).

RNA extraction and analysis

Total RNA was extracted from mouse testes using the ReliaPrep^{TM} RNA Tissue Miniprep System (Promega, USA) or TRIzol reagent (Thermo Fisher Scientific, USA) following the manufacturers' instructions. Purified RNA was reverse transcribed into cDNA using a GoScript^{TM} Reverse Transcription Kit (Promega, USA). Subsequently, reverse transcription-quantitative real-time polymerase chain reaction (RT-qPCR) analysis was performed using a SYBR Green RT-qPCR Kit (TransGen, China) on the LightCycler 96 platform (Roche, Switzerland). Relative transcript levels were calculated using the $2^{-\Delta\Delta Ct}$ method with normalization to ribosomal protein L19 (*Rpl19*). Primer sequences used for RT-qPCR are detailed in Supplementary Table S2. For RNA sequencing (RNA-seq), testicular samples were collected from cKO and control mice at postnatal day 10 (P10), with each biological replicate comprising pooled tissue from three mice. RNA extraction and downstream sequencing analysis were

performed by NeoRibo Biotechnology Co., Ltd. (China).

Immunofluorescence staining and histological analysis

Testes from cKO and control mice were preserved in 4% (w/v) paraformaldehyde (PFA) at 4°C for 12–24 h, followed by graded alcohol dehydration, xylene clearing, and paraffin embedding. Paraffin blocks were sectioned at 5 μm thickness and dried at 42°C for 12 h. Sections were then dewaxed, rehydrated, and underwent antigen retrieval using a 10 mM citrate buffer (pH 5.0–6.0). Non-specific binding was minimized by incubation with 10% (v/v) standard donkey serum at 37°C for 1 h. Sections were then incubated with primary antibodies at 4°C for 12–24 h, followed by incubation with secondary antibodies conjugated to Alexa Fluor-488, -555, or -647 (1:200; Thermo Fisher Scientific, USA) at 37°C for 1–2 h. Details of primary antibodies are listed in Supplementary Table S3. Nuclei were counterstained using 4′,6-diamidino-2-phenylindole (DAPI), and fluorescence images were acquired using a confocal microscope (LSM 800, Zeiss, Germany). For histological evaluation, paraffin-embedded testicular sections (5 μm) were stained with hematoxylin and eosin (H&E).

Western blotting

Proteins were extracted from mouse testes using RIPA lysis buffer (Beyotime, China), and 20 μg of total protein was used for each analysis. Protein samples were separated using sodium dodecyl sulfate-polyacrylamide gel electrophoresis (SDS-PAGE) and transferred onto polyvinylidene difluoride (PVDF) membranes (Merck-Millipore, Germany). To block non-specific binding, membranes were placed in 5% (w/v) milk or BSA at 37°C for 1 h or 4°C for 12 h, followed by incubation with primary antibodies (Supplementary Table S3) for 12–24 h at 4°C. Membranes were washed using Tris-buffered saline containing 0.1% (v/v) Tween-20 (TBST) and then incubated with horseradish peroxidase HRP-conjugated secondary antibodies (1:10 000; ZSGB, China). Blots were probed using NcmECL Ultra reagent (NCM Biotech, China) and visualized using the Tanon 5200 multi-chemiluminescent imaging system (Tanon, China). Grayscale values of protein blots were quantified using ImageJ software (NIH Image, Bethesda, USA), with α-Tubulin or GAPDH serving as internal controls.

Coomassie brilliant blue staining

Proteins extracted from mouse testes were separated by SDS-PAGE and stained using Coomassie brilliant blue solution composed of 1% Coomassie brilliant blue R250, 40% ethanol, and 10% acetic acid for 20 min at 37°C. Gels were subsequently heated in a boiling water bath for 30 min for decolorization.

Nuclear and cytoplasmic extracts

Nuclear and cytoplasmic protein fractions were prepared from mouse testes using NE-PER^{TM} Nuclear and Cytoplasmic Extraction Reagents (Thermo Fisher Scientific, USA), according to the manufacturer's protocols. Histone H3 was used as a nuclear marker, whereas glyceraldehyde-3-phosphate dehydrogenase (GAPDH) was used as a cytoplasmic marker.

Ribosome sequencing (Ribo-seq) analysis

Ribo-seq was conducted using testicular samples collected from cKO and control mice at P10, with each sample comprising pooled tissue from three mice. Ribosomes were isolated and processed by NeoRibo Biotechnology Co., Ltd. using a QEZ-seq® 1.0 Kit (1012S, NeoRibo, China) to generate high-resolution profiles of ribosome-protected mRNA fragments. Adapter sequences were removed from raw sequencing reads using Cutadapt and reads with lengths ranging from 25 to 35 bp were retained for downstream analysis. Ribosomal RNA-derived reads were removed by alignment to rRNA reference sequences using Bowtie, and the remaining reads were aligned to the GRCm38 reference genome using STAR. Trinucleotide periodicity and codon usage were analyzed using the revised riboWaltz package. Read counts were calculated using featureCounts and subsequently normalized using the DESeq2 package. Translational efficiency was determined as the ratio of normalized ribosome profiling abundance to normalized RNA-seq abundance, as reported previously (Duan et al., 2022; Su et al., 2022). Differential translational efficiency was estimated using the DESeq2 package, with genes exhibiting fold change≥1.5 and P-value<0.05 considered significant. Functional enrichment analyses, including Gene Ontology (GO) and Kyoto Encyclopedia of Genes and Genomes (KEGG), were performed using the cluster Profiler package in R.

Terminal deoxynucleotidyl transferase-mediated 2'-deoxyuridine 5'-triphosphate (dUTP) nick-end labeling (TUNEL) assay

Apoptosis in testicular sections was evaluated using a TUNEL kit (12156792910, Roche). Sections were first rehydrated in PBS and fixed in 4% (w/v) PFA. Membrane permeabilization was performed using 0.5% (v/v) Triton X-100, followed by incubation with TUNEL reaction mixture according to the manufacturer's instructions. After PBS washing, nuclei were counterstained with DAPI. Fluorescence signals were visualized using a confocal microscope (LSM 800, Zeiss, Germany).

5-Bromo-2-deoxyuridine (BrdU) incorporation assay

For BrdU incorporation analysis, mice received an intraperitoneal injection of BrdU (B5002, Sigma-Aldrich, USA; 10 mg/mL, 10 μL/g body weight) 4 h before sacrifice (Mazzitelli et al., 2022). Animals were deeply anesthetized and euthanized by cervical dislocation.

Evaluation of reactive oxygen species (ROS) levels

Testes collected from P10 mice were minced into small pieces using microsurgical scissors and digested at 37°C for 15–30 min in the presence of collagenase type IV (C5138, Sigma-Aldrich, USA;1 mg/mL) and 0.25% (w/v) trypsin (T1426, Sigma-Aldrich, USA). Enzymatic digestion was terminated by the addition of fetal bovine serum (FBS). Cell suspensions were filtered through a 50 μm filter and centrifuged at 1 200 ×g for 3 min at 4°C. THY1$^+$ cells were isolated by magnetic-activated cell sorting (MACS) and collected by centrifugation at 1 200 ×g for 3 min at 4°C. Cell precipitates were resuspended in serum-free DMEMα containing 10 μmol/L 2',7'-dichlorodihydrofluorescein diacetate (DCFH-DA) (S0033S, Beyotime, China) and incubated in a 37°C cell incubator for 30 min, with gentle mixing every 3–5 min to ensure uniform probe loading. Cells were then washed three times with serum-free DMEMα cell culture medium to remove excess extracellular DCFH-DA. For GC-1 cells, serum-free DMEMα containing 10 μmol/L DCFH-DA was added directly to the culture dishes, and cells were stained for 30 min, followed by three washes with serum-free DMEMα cell culture medium.

Puromycin incorporation assay

Protein synthesis was assessed by puromycin incorporation into nascent peptides. For *in vivo* puromycin labeling, mice were administered intraperitoneal injections of puromycin (ST551, Beyotime, China; 10 mg/mL, 10 μL/g body weight) 1 h before sacrifice. Animals were deeply anesthetized and euthanized by cervical dislocation.

Cell culture and treatment

Mouse-derived spermatogonial GC-1 spg cells (Procell Biotechnology, China) were cultured in DMEMα supplemented with 1% (v/v) penicillin-streptomycin and 10% (v/v) FBS. Cells were cultured and passaged at 37°C in a humidified atmosphere containing 5% CO_2. For pharmacological treatment, cells were exposed to 10 μmol/L 2-(benzylsulfonyl)-1-(1H-indol-3-yl)-1,2-dihydroisoquinoline (IBR2), a specific RAD51 inhibitor, 0.025 μmol/L thapsigargin (TG), an endoplasmic reticulum stress inducer, or 200 μmol/L H_2O_2 for 48 h. Drug concentrations were determined based on previous studies (Chu et al., 2022; Wang et al., 2014; Zhu et al., 2015). For immunofluorescence analysis, GC-1 cells cultured on cell-climbing slides were fixed with 4% PFA or precooled methanol for 15–30 min at room temperature, followed by permeabilization with 0.3% (v/v) Triton X-100 for 15 min. Non-specific binding was blocked with 5% (v/v) BSA for 2 h at room temperature. Cells were then incubated with the indicated primary antibodies overnight at 4°C. After three washes with PBS, each for 5 min, cells were incubated with appropriate fluorescence-conjugated secondary antibodies for 1–2 h at 37°C in the dark. Slides were then washed three additional times with PBS, and nuclei were counterstained with DAPI for 10 min at room temperature. Coverslips were mounted using an anti-fluorescence quencher and examined using a confocal microscope (LSM 800, Zeiss, Germany), with representative images captured for analysis.

For cell viability assays, GC-1 cells were seeded into 96-well plates, and viability was detected after 48 h of treatment using Cell Counting Kit-8 (CCK-8) (C0038, Beyotime, China) with a microplate reader (Bio-Rad, USA) according to the manufacturer's instructions and previous research (Zhang et al., 2022b). For EdU incorporation assays, 10 μmol/L EdU was added to culture medium 8 h before fixation.

Cell transfection and rescue experiments

For gene silencing, GC-1 cells were transfected with small interfering RNAs (siRNAs; Gene Pharma, China) targeting *Eif5* (si-*Eif5*) or with a negative control (si-NC) using Lipofectamine 2000 (Invitrogen, USA). For overexpression assays, pcDNA3.1-NC (negative control) and pcDNA3.1-Flag-RAD51 (plasmid expressing Flag-labeled RAD51) were obtained from Beijing Genomics Institute (China) and transfected into GC-1 cells using X-tremeGENE HP DNA Transfection Reagent (Roche, Switzerland) following the manufacturer's protocols. For rescue experiments, cells were treated with 1 μmol/L rapamycin (Bai et al., 2020) or 5 mmol/L N-acetylcysteine (NAC) (Cocetta et al., 2021) for 48 h.

Statistical analysis

Each experiment was performed at least three times to ensure accuracy. Seminiferous tubules with comparable lumen size were selected for quantification of different spermatogonial populations per tubule. Statistical analyses were performed using GraphPad Prism v.8.0.1 (GraphPad Prism, USA). Data are presented as mean±standard deviation (SD), with individual data points superimposed on mean values. Unless otherwise stated, statistical significance was assessed using two-tailed unpaired Student's *t*-tests (ns: Not significant; *: $P<0.05$; **: $P<0.01$; ***: $P<0.001$).

RESULTS

***Eif5* deletion in male mouse germ cells causes spermatogenic failure and infertility**

Spatiotemporal expression analysis showed a progressive increase in eIF5 mRNA and protein abundance in testes from P1 to P35 (Figure 1A, B). Immunofluorescence staining further demonstrated strong eIF5 expression in germ cells positive for germ cell nuclear antigen 1 (GCNA1^{+}), whereas only weak signals were detected in Leydig cells (3β-HSD^{+}) and Sertoli cells (SOX9^{+}) (Figure 1C; Supplementary Figure S1A, B). Consistent with these observations, both mRNA and protein levels of eIF5 were significantly higher in germ cells, including spermatogonia and spermatocytes, than in somatic cells such as Leydig and Sertoli cells (Figure 1A, B; Supplementary Figure S1C). Immunofluorescence analysis together with nucleocytoplasmic fractionation showed that eIF5 was predominantly localized in the cytoplasm of undifferentiated spermatogonia positive for promyelocytic leukemia zinc finger (PLZF^{+}), differentiating spermatogonia positive for KIT proto-oncogene receptor tyrosine kinase (KIT^{+}), and spermatocytes positive for synaptonemal complex protein 3 (SYCP3^{+}) (Supplementary Figure S1A, D). These results indicate that eIF5 is prominently expressed in male germ cells and may be involved in regulating spermatogenesis.

To define the contribution of eIF5 to this process, male germ cell-specific *Eif5* cKO mice were generated by mating *Eif5*$^{fl/fl}$ (control) mice with *Stra8*-Cre mice (Lu et al., 2022). Efficient loss of *Eif5* in testes from cKO mice was verified by RT-qPCR and western blotting (Figure 1D, E). Cell type-specific deletion was further examined by co-staining eIF5 with GDNF family receptor alpha 1 (GFRα1), a marker of stem-like spermatogonia, SRY-box transcription factor 3 (SOX3), a marker of progenitor spermatogonia, KIT, a marker of differentiating spermatogonia, and SYCP3, a marker of spermatocytes. These analyses showed that *Eif5* deletion occurred in SOX3^{+} progenitor spermatogonia, KIT^{+} differentiating spermatogonia, and SYCP3^{+} spermatocytes (Figure 1F; Supplementary Figure S2A). Double-immunofluorescence staining further demonstrated STRA8 expression in SOX3^{+} progenitor spermatogonia (Supplementary Figure S2B). Although cKO males exhibited normal gross appearance and survival (Figure 1G), they were completely infertile. Testis weight in adult cKO mice was markedly reduced compared with controls, and histological examination revealed seminiferous tubules with pronounced germ cell depletion and complete absence of elongating spermatids (Figure 1H–J). Consistent with these defects, no sperm were detected in epididymal samples from cKO mice (Figure 1J). Taken together, these findings show that loss of *Eif5* in male germ cells severely disrupts spermatogenesis by reducing germ cell abundance and ultimately causing infertility.

***Eif5* deletion in male germ cells reduces the abundance of SOX3^{+} progenitor spermatogonia**

To determine whether *Eif5* deletion in male germ cells affects meiotic progression and spermatocyte formation,

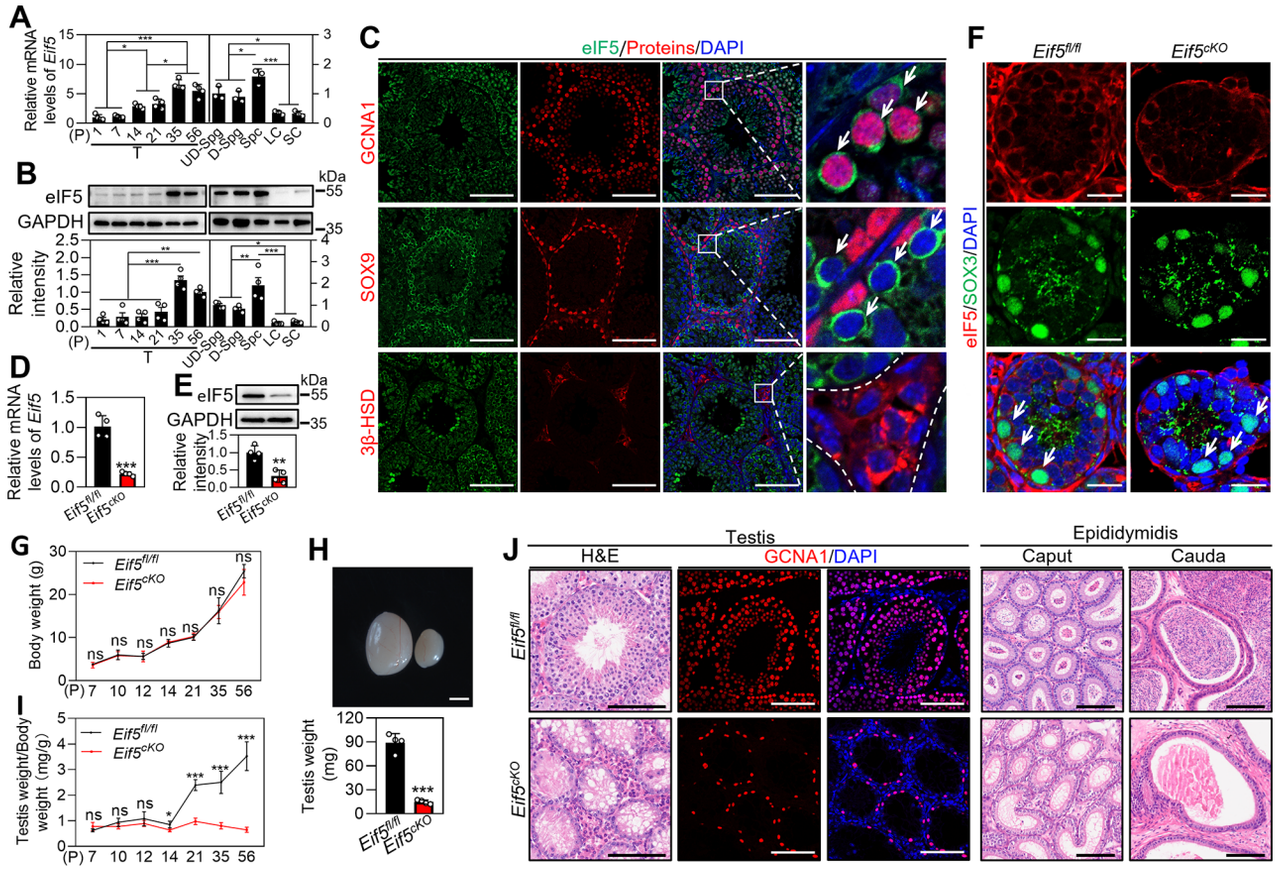

Figure 1 *Eif5* deletion in male mouse germ cells induces spermatogenic defects and infertility

A, B: eIF5 mRNA (A) and protein (B) levels in testes collected at different postnatal stages and in isolated testicular cell populations. GAPDH was used as an internal control. T, testis; UD-Spg, undifferentiated spermatogonia; D-Spg, differentiating spermatogonia; Spc, spermatocyte; LC, Leydig cells; SC, Sertoli cells; P, postnatal day. In the left panel of B, values are presented relative to eIF5 levels in testes at P56, which were set to 1. In the right panel of B, values are presented relative to eIF5 levels in undifferentiated spermatogonia, which were set to 1. C: Double-immunofluorescence staining of eIF5 (green) with GCNA1 (germ cell marker, red), SOX9 (Sertoli cell marker, red), or 3β-HSD (Leydig cell marker, red) in adult mouse testis sections. White arrowheads indicate representative germ cells. Nuclei were counterstained with DAPI (blue). D–F: Validation of *Eif5* knockout efficiency in testes from cKO and control mice at P10 by RT-qPCR (D), western blotting (E), and double-immunofluorescence staining for eIF5 (red) and SOX3 (progenitor spermatogonia marker, green) (F). White arrowheads indicate representative SOX3$^+$ progenitor spermatogonia. G–I: Comparison of body weight at different postnatal stages (G), testis morphology at P56 (H), and testicular index at different postnatal stages (I) between cKO and control mice. J: Immunofluorescence staining for GCNA1 (red) in testis sections, and hematoxylin and eosinstaining of testis and epididymis sections from adult cKO and control mice. For A, B, D, E, and G–I, n=3–4 independent experiments. Scale bars: C and J, 100 μm; F, 20 μm; H, 2 000 μm. For A and B, P-values were determined by one-way analysis of variance (ANOVA) followed by Tukey's test. ns: Not significant; *: P<0.05; **: P<0.01; ***: P<0.001.

immunofluorescence staining for SYCP1 and SYCP3 was conducted on testes collected from P10 to P21 mice. A progressive reduction in SYCP1$^+$ and SYCP3$^+$ cells was observed in cKO testes across this developmental interval, indicating severe impairment of meiotic progression following *Eif5* deletion in male germ cells (Figure 2A). Prior to entry into meiosis, spermatogonia undergo multiple rounds of mitotic proliferation (Feng et al., 2022). Quantification of spermatogonial populations demonstrated that both undifferentiated spermatogonia (PLZF$^+$) and differentiating spermatogonia (KIT$^+$) were significantly reduced in testes from P10 cKO mice compared with controls (Figure 2B, C; Supplementary Figure S3A). The undifferentiated spermatogonial population includes SSCs with self-renewal capacity and progenitor spermatogonia that are committed to differentiation (Di Persio et al., 2021; Liu et al., 2022; Thirouard et al., 2022). Further analysis of spermatogonial subpopulations showed that the number of GFRα1$^+$ stem-like spermatogonia was not significantly altered, whereas SOX3$^+$ progenitor spermatogonia were significantly decreased in the testes of P10 cKO mice (Figure 2B, C; Supplementary Figure S3A). Consistent with these results, protein levels of PLZF, KIT, and SOX3 were significantly decreased in the testes of P10 cKO mice (Figure 2D). Furthermore, RT-qPCR analysis showed that *Kit* and *Sox3* mRNA expression levels were significantly reduced in the testes of P10 cKO mice compared with controls (Supplementary Figure S3B). Collectively, these results indicate that *Eif5* deletion in male germ cells primarily disrupts the progenitor spermatogonial population, which likely leads to reduced differentiating spermatogonia and subsequent meiotic defects.

Eif5 deletion suppresses proliferation and promotes apoptosis in SOX3$^+$ progenitor spermatogonia

The impact of *Eif5* deletion on spermatogonial proliferation

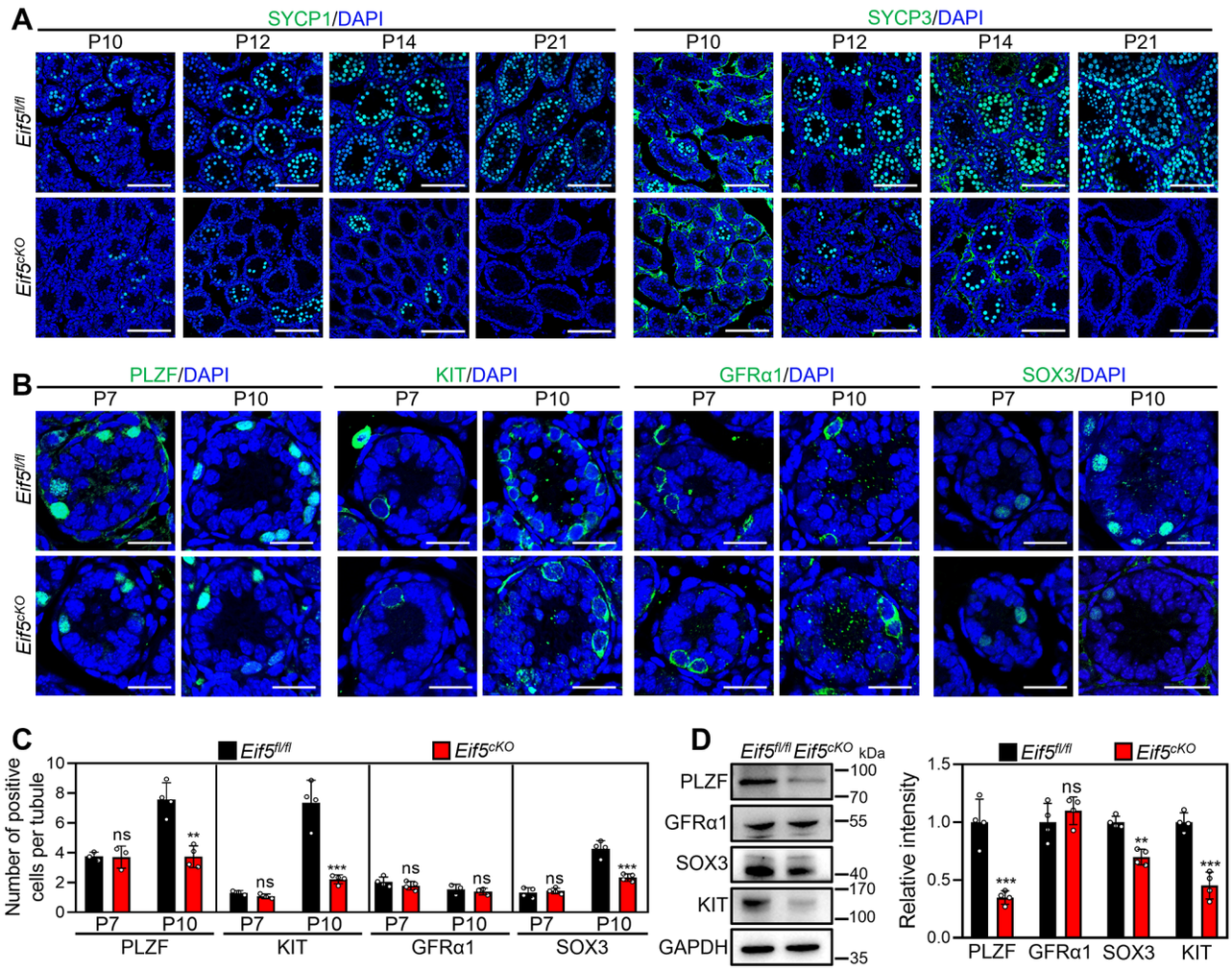

Figure 2 ***Eif5*** **deletion in male germ cells reduces SOX3$^+$ progenitor spermatogonia abundance**

A: Immunofluorescence staining for SYCP3 (green) or SYCP1 (green) in testes from cKO and control mice at different postnatal stages. Nuclei were counterstained with DAPI (blue). B: Immunofluorescence staining for PLZF (undifferentiated spermatogonia marker, green), KIT (differentiating spermatogonia marker, green), GFRα1 (stem-like spermatogonial marker, green), and SOX3 (progenitor spermatogonia marker, green) in testes from cKO and control mice at P7 and P10. C: Quantification of PLZF$^+$, KIT$^+$, GFRα1$^+$, and SOX3$^+$ cells per seminiferous tubule in testes from cKO and control mice at P7 and P10. Tubules with similar lumen size were counted. D: Western blot analysis of PLZF, GFRα1, SOX3, and KIT protein levels in testes from cKO and control mice at P10. GAPDH was used as an internal control. For C, more than 200 tubules from 3–4 independent experiments were analyzed in each group. For D, n=4 independent experiments. Scale bars: A, 100 μm; B, 25 μm. ns: Not significant; *: P<0.05; **: P<0.01; ***: P<0.001.

and apoptosis was evaluated using immunofluorescence staining and western blotting. In testes from P10 cKO mice, the proportions of Ki-67$^+$ and BrdU$^+$ cells within SOX3$^+$ progenitor spermatogonia and KIT$^+$ differentiating spermatogonia were significantly decreased compared with controls (Figure 3A, B; Supplementary Figure S4A), indicating impaired proliferative activity. In contrast, the percentage of seminiferous tubules containing Cleaved Caspase-3$^+$ and TUNEL$^+$ signals was significantly increased in the testes of P10 cKO mice compared with controls (Figure 3A, C; Supplementary Figure S4B), demonstrating enhanced apoptosis. Consistent with these observations, *Eif5* deletion in male germ cells resulted in increased levels of pro-apoptotic proteins, including PDCD7, PUMA, and Cleaved Caspase-3, accompanied by decreased levels of anti-apoptotic proteins BCL-2 and BCL-xL in testes from P10 mice (Figure 3D). These results suggest that *Eif5* deficiency suppresses proliferation and promotes apoptosis in SOX3$^+$ progenitor spermatogonia, likely contributing to impaired spermatogonial differentiation.

Eif5 deletion disrupts transcriptional and translational regulation in mouse testes

To investigate the effects of *Eif5* deletion on transcription and translation, global protein synthesis, Ribo-seq, and RNA-seq were performed using testes from P10 cKO and control mice. Newly synthesized proteins were labeled using puromycin, which incorporates into nascent peptide chains. Immunofluorescence staining and western blot detection of puromycin incorporation demonstrated that *Eif5* deletion markedly reduced global protein synthesis in SOX3$^+$ progenitor spermatogonia and KIT$^+$ differentiating spermatogonia (Figure 4A–C; Supplementary Figure S5A–C). Quality assessment of Ribo-seq reads showed expected read length distribution (Figure 4D), clear trinucleotide periodicity (Supplementary Figure S6A), and predominant mapping of reads to coding sequences of protein-coding genes (Figure 4E), confirming high data reliability. Ribo-seq analysis

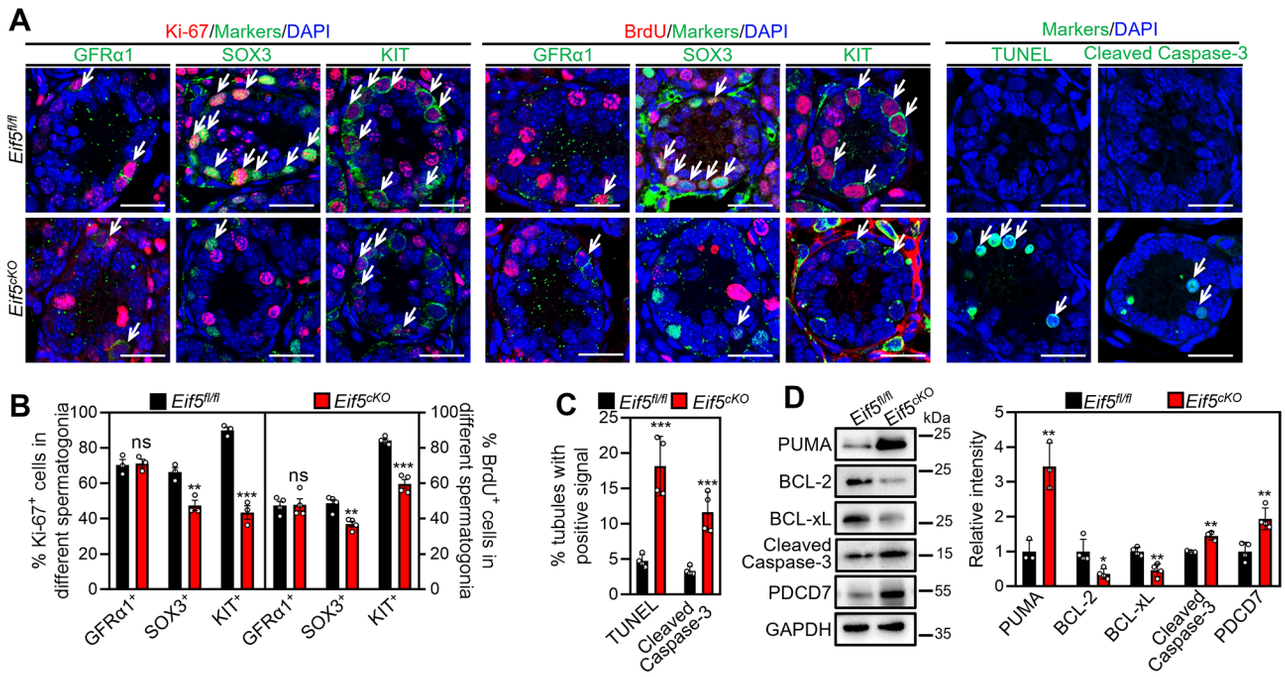

Figure 3 *Eif5* deletion suppresses proliferation and promotes apoptosis in SOX3$^+$ progenitor spermatogonia

A: Double-immunofluorescence staining for GFRα1 (green), SOX3 (green), or KIT (green) together with Ki-67 (red) or BrdU (red), as well as TUNEL (green) and immunofluorescence staining for Cleaved Caspase-3 (green), in testes from cKO and control mice at P10. Nuclei were counterstained with DAPI (blue). White arrowheads indicate representative double-positive cells or apoptotic cells. Scale bars: 25 μm. B: Percentage of Ki-67$^+$ or BrdU$^+$ cells within GFRα1$^+$, SOX3$^+$, and KIT$^+$ populations in testes from cKO and control mice at P10. C: Percentage of seminiferous tubules containing Cleaved Caspase-3- and TUNEL-positive signals in testes from cKO and control mice at P10. D: Western blot analysis of PUMA, BCL-2, BCL-xL, Cleaved Caspase-3, and PDCD7 protein levels in testes from cKO and control mice at P10. GAPDH was used as an internal control. For B, more than 300 cells from 3–4 independent experiments were analyzed in each group. For C, more than 400 tubules from four independent experiments were analyzed in each group. For D, *n*=3–4 independent experiments. ns: Not significant; *: P<0.05; **: P<0.01; ***: P<0.001.

identified 753 differentially translated genes (DTGs), including 481 down-regulated and 272 up-regulated genes, in testes from cKO mice (Figure 4F). Protein levels of representative DTGs were validated by western blotting (Supplementary Figure S6B). GO enrichment analysis showed that down-regulated DTGs were predominantly associated with DNA repair, germ cell development, G2/M transition of mitosis, autophagy, ubiquitin ligase and transferase activity, and translation in testes from cKO mice (Figure 4G). In contrast, up-regulated DTGs were primarily enriched in apoptotic processes, calcium ion homeostasis, GTPase activity, oxidative stress, and cellular response to unfolded protein (Figure 4G). Because GO analysis indicated enrichment of ubiquitin ligase and transferase activity among down-regulated DTGs, ubiquitination-related DTGs were further explored using Venn diagram comparison. This analysis identified 49 ubiquitination-related DTGs, including 39 down-regulated and 10 up-regulated genes (Figure 4H), suggesting reduced ubiquitination activity in the testes of cKO mice. Integration of Ribo-seq and RNA-seq datasets revealed 2 017 differentially translated efficiency genes (DTEGs), including 1 007 down-regulated and 1 010 up-regulated genes, in the testes of cKO mice (Supplementary Figure S6C). Consistent with DTG enrichment results, down-regulated DTEGs were associated with DNA repair, autophagy, protein ubiquitination, and translation, while up-regulated DTEGs were related to unfolded protein binding, calcium ion homeostasis, and detection of stimulus in the testes of cKO mice (Figure 4I). These results indicate that global alterations in translation are partially attributable to changes in translation efficiency, and these functional impairments may contribute to spermatogenesis defects in the testes of cKO mice.

RNA-seq analysis identified 1 575 differentially expressed transcripts, including 1 170 down-regulated and 405 up-regulated transcripts, in the testes of P10 cKO mice (Supplementary Figure S6D). Altered expression of representative transcripts was validated by RT-qPCR (Supplementary Figure S6E). Among these transcripts, 17 down-regulated and three up-regulated transcripts were also detected in spermatogonia with low *EIF5* expression from seven iNOA patients (Supplementary Figure S6F) (Chen et al., 2023). Down-regulated transcripts included *Adad1*, *Apitd1*, *Ccdc54*, *Cdkn3*, *Cenpu*, *Cox17*, *Dkkl1*, *Dll3*, *Dpm1*, *Gapdhs*, *Htatip2*, *Oip5*, *Prr30*, *Spa17*, *Spata33*, *Syce3*, and *Ube2t*, whereas up-regulated transcripts included *Cbfa2t3*, *Etv5*, and *Peg10*. Aberrant expression of these genes may contribute to the development of iNOA.

Eif5 deletion enhances ER stress in SOX3$^+$ progenitor spermatogonia

In SOX3$^+$ progenitor spermatogonia and KIT$^+$ differentiating spermatogonia from P10 cKO mice, fluorescence intensity of ubiquitin, microtubule-associated protein light chain 3B (LC3B), and insulin-like growth factor 2 receptor (IGF2R) was significantly reduced, whereas fluorescence intensity of sequestosome 1 (SQSTM1), an autophagy substrate, and the proportion of activating transcription factor 4 (ATF4)-positive cells, a marker of ER stress, were significantly increased compared with controls (Figure 5A–C; Supplementary Figures S7A, B, S8A, S9A, B). In THY1$^+$ cells isolated from the testes of P10 cKO mice, fluorescence intensity of calnexin, an ER

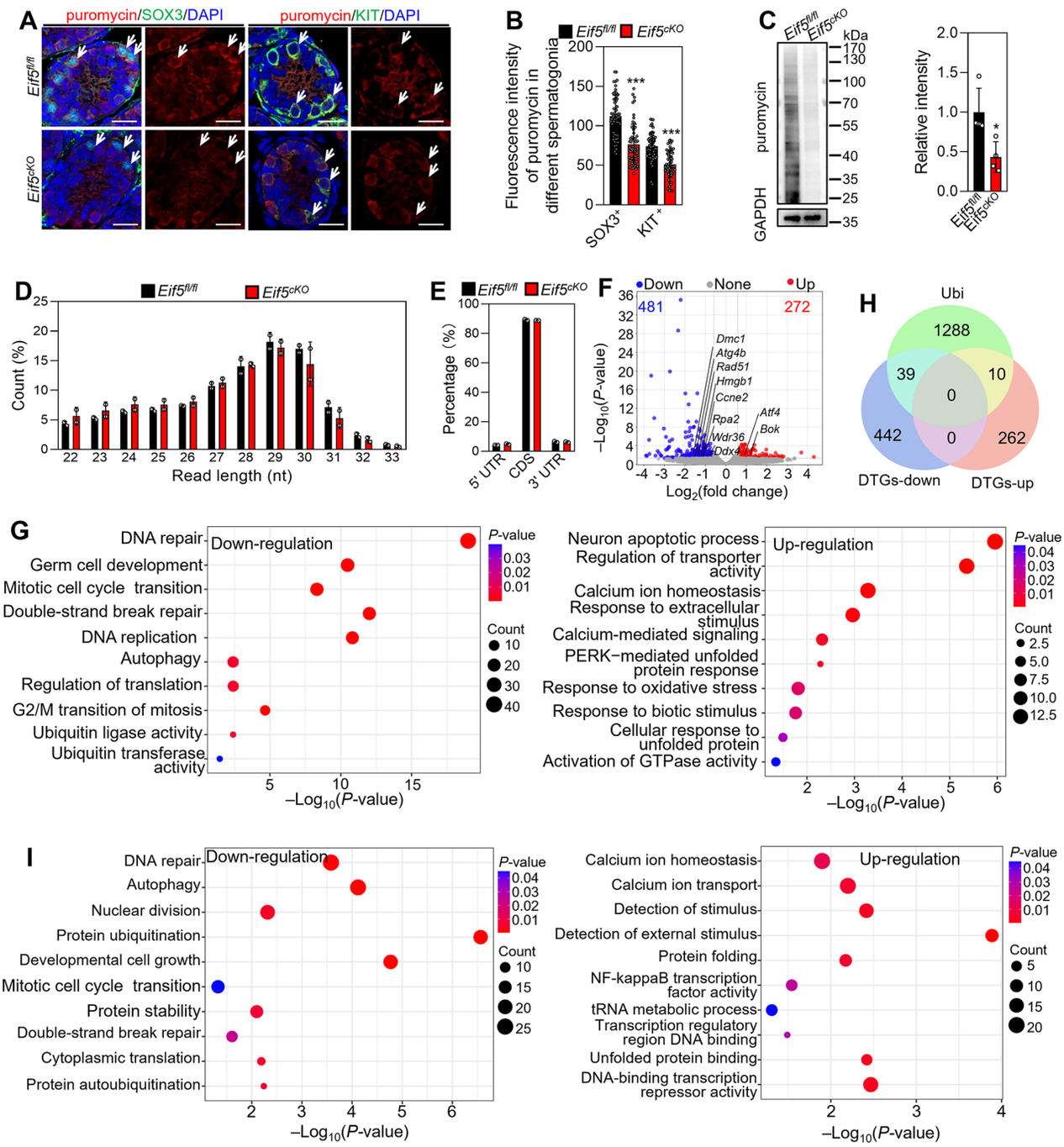

Figure 4 ***Eif5*** **deletion disrupts transcriptional and translational regulation in mouse testes**

A: Double-immunofluorescence staining for puromycin (red) together with SOX3 or KIT (green) in testes from cKO and control mice at P10. Nuclei were counterstained with DAPI (blue). White arrowheads indicate representative double-positive cells. Scale bars: 25 μm. B: Quantification of puromycin fluorescence intensity in $SOX3^+$ and KIT^+ cells. C: Western blot analysis of puromycin levels in testes from cKO and control mice at P10. GAPDH was used as an internal control. D: Read length distribution of Ribo-seq reads. E: Genomic distribution of Ribo-seq reads across different transcript regions. F: Volcano plot showing differentially translated genes (DTGs) in testes from cKO and control mice at P10. Genes with fold-change≥1.5 and *P*-value<0.05 were selected for analysis. G: Bubble plots showing enriched GO terms for significantly down-regulated (left) and up-regulated (right) DTGs identified by Ribo-seq in testes from cKO and control mice. H: Venn diagram showing overlap among up-regulated and down-regulated DTGs and ubiquitination-related genes. Ubiquitination-related genes were obtained from the Integrated Annotations for Ubiquitin and Ubiquitin-like Conjugation Database (iUUCD; http://iuucd.biocuckoo.org/). Ubi, ubiquitin. I: Bubble plots showing enriched GO terms for significantly down-regulated (left) and up-regulated (right) DTEGs identified by Ribo-seq and RNA-seq in testes from cKO and control mice. For B, $SOX3^+$ and KIT^+ cells from 60 tubules in three independent experiments were analyzed, with each data point representing mean fluorescence intensity of puromycin in $SOX3^+$ or KIT^+ cells of a single tubule. For C, n=4 independent experiments. *: P<0.05; **: P<0.01; ***: P<0.001.

marker, was significantly increased, and calnexin distribution appeared uneven with nuclear-associated localization compared with controls (Figure 5A). Furthermore, RT-qPCR analysis demonstrated that *Eif5* deletion in male germ cells increased mRNA levels of *Trib3*, a downstream target of ATF4, in testes from P10 mice (Figure 5D). Consistent with

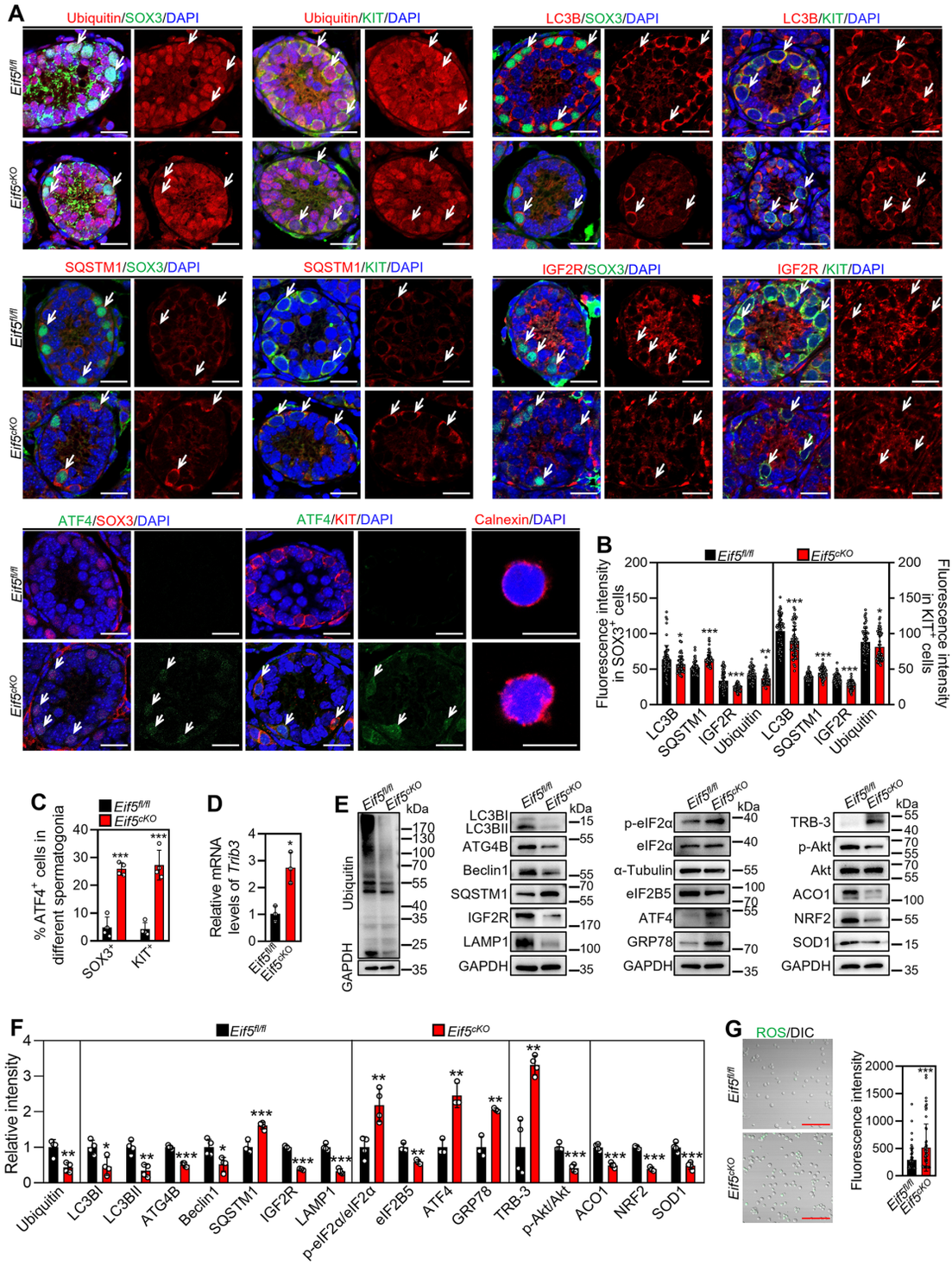

Figure 5 *Eif5* deletion enhances ER stress in SOX3$^+$ progenitor spermatogonia

A: Double-immunofluorescence staining for ubiquitin, LC3B, SQSTM1, IGF2R, or ATF4 together with SOX3 or KIT in testes from cKO and control mice at P10, and immunofluorescence staining of calnexin in THY1$^+$ cells from testes of cKO and control mice at P10. Nuclei were counterstained with DAPI. White arrowheads indicate representative double-positive cells. B: Quantification of ubiquitin, LC3B, SQSTM1, and IGF2R fluorescence intensity in SOX3$^+$ and KIT$^+$ cells. C: Percentage of ATF4$^+$ cells within SOX3$^+$ and KIT$^+$ populations in testes from cKO and control mice at P10. D: RT-qPCR analysis of *Trib3* in testes from cKO and control mice at P10. E, F: Western blot analysis of ubiquitin, LC3B I/II, ATG4B, Beclin1, SQSTM1, IGF2R, LAMP1, p-eIF2α, eIF2α, eIF2B5, ATF4, GRP78, TRB-3, p-Akt, Akt, ACO1, NRF2, and SOD1 protein levels in testes from cKO and control mice at P10. GAPDH or α-Tubulin served as the internal control. G: Fluorescence staining and quantification of ROS using DCFH-DA (green) in THY1$^+$ cells from cKO and control mice at P10. For B, SOX3$^+$ and KIT$^+$ cells from 60 tubules across three independent experiments were analyzed, with each data point representing mean fluorescence intensity of the target protein in SOX3$^+$ or KIT$^+$ cells of a single tubule. For C, more than 300 cells from four independent experiments were analyzed in each group. For D and F, n=3–4 independent experiments. For G, more than 300 cells from three independent experiments were analyzed in each group, with every five cells averaged as one data point. Scale bars: A, 10 μm for calnexin and 20 μm for others; G, 100 μm. *: P<0.05; **: P<0.01; ***: P<0.001.

these observations, *Eif5* deletion in male germ cells reduced levels of ubiquitin, eIF2B5, autophagy-related proteins, including LC3B I/II, Beclin1, IGF2R, and LAMP1, proliferation-related protein p-Akt, and antioxidant-related proteins, including aconitase 1 (ACO1, a key antioxidant protein), superoxide dismutase 1 (SOD1, a homodimeric cytosolic antioxidant) and NRF2, while increasing levels of SQSTM1 and ER stress-related proteins including p-eIF2α, ATF4, GRP78, and TRB-3 in the testes of P10 mice (Figure 5E, F). In addition, ROS levels were significantly elevated in THY1$^+$ cells from testes of P10 cKO mice compared with controls (Figure 5G). These findings indicate that *Eif5* deletion reduces ubiquitination and autophagy activity, likely resulting in excessive ER stress in SOX3$^+$ progenitor spermatogonia and KIT$^+$ differentiating spermatogonia.

Eif5 deletion induces DNA damage and cell cycle arrest in SOX3$^+$ progenitor spermatogonia

The effects of *Eif5* deletion on DNA repair capacity in spermatogonial populations were further examined. In SOX3$^+$ progenitor spermatogonia and KIT$^+$ differentiating spermatogonia from P10 cKO mice, fluorescence intensity of DNA repair protein RAD51 homolog 1 (RAD51) and replication protein A2 (RPA2) was markedly reduced, whereas fluorescence intensity of the DNA damage marker γH2AX and the proportion of cells positive for the G2/M phase marker histone H3 pSer10 were significantly increased compared with controls (Figure 6A–C; Supplementary Figures S10A–D, S11A–D). These findings indicate accumulation of DNA damage accompanied by cell cycle arrest at the G2/M phase. Consistent with these observations, protein analysis showed that *Eif5* deletion in male germ cells reduced levels of DNA repair-associated proteins RAD51 and RPA2 and the G2/M transition regulator aurora kinase B (AURKB), while increasing

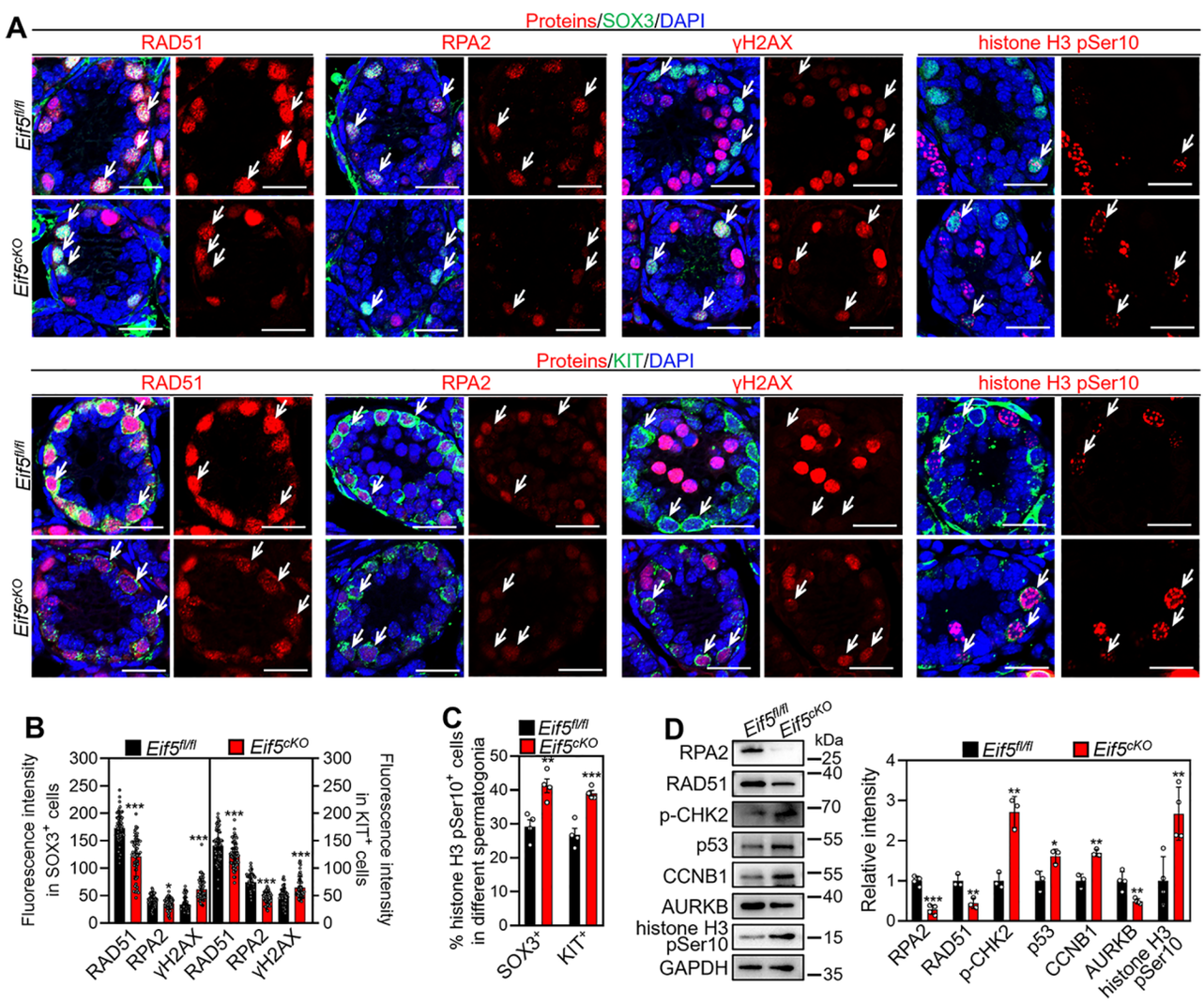

Figure 6 ***Eif5*** **deletion induces DNA damage and cell cycle arrest in SOX3$^+$ progenitor spermatogonia**

A: Double-immunofluorescence staining for RAD51, RPA2, γH2AX, and histone H3 pSer10 (red) together with SOX3 or KIT (green) in testes from cKO and control mice at P10. Nuclei were counterstained with DAPI (blue). White arrowheads indicate representative double-positive cells. Scale bars: 25 μm. B: Quantification of RAD51, RPA2, and γH2AX fluorescence intensity in SOX3$^+$ and KIT$^+$ cells. C: Percentage of histone H3 pSer10$^+$ cells within SOX3$^+$ and KIT$^+$ populations in testes from cKO and control mice at P10. D: Western blot analysis of RPA2, RAD51, p-CHK2, p53, CCNB1, AURKB, and histone H3 pSer10 levels in testes from cKO and control mice at P10. GAPDH was used as an internal control. For B, SOX3$^+$ and KIT$^+$ cells from 60 tubules across three independent experiments were analyzed, with each data point representing mean fluorescence intensity of the target protein in SOX3$^+$ and KIT$^+$ cells of a single tubule. For C, more than 300 SOX3$^+$ and KIT$^+$ cells across four independent experiments were analyzed in each group. For D, n=3–4 independent experiments. *: P<0.05; **: P<0.01; ***: P<0.001.

levels of DNA damage response proteins p-CHK2 and p53 as well as G2/M phase marker proteins cyclin B1 (CCNB1) and histone H3 pSer10 in testes from P10 mice (Figure 6D). The results suggest that *Eif5* deletion impairs DNA repair mechanisms, leading to accumulation of DNA damage and subsequent cell cycle arrest in SOX3$^+$ progenitor spermatogonia and KIT$^+$ differentiating spermatogonia.

Eif5 knockdown-induced DNA damage and apoptosis are partially rescued by RAD51 overexpression, rapamycin, and NAC in GC-1 cells

To clarify the mechanistic relationship among ER stress, DNA repair deficiency, and apoptosis in *Eif5*-deficient spermatogonia, rescue experiments were performed in the mouse spermatogonial cell line GC-1 following si-*Eif5* treatment. Cells were transfected with pcDNA3.1-Flag-RAD51 plasmid and treated with rapamycin, an autophagy activator, or NAC, a ROS scavenger. *Eif5* knockdown reduced cell proliferation and DNA repair capacity while increasing ER stress, DNA damage, and apoptosis in GC-1 cells (Figure 7A–F). RAD51 overexpression as well as rapamycin and NAC treatment partially rescued DNA damage and apoptosis in *Eif5* knockdown GC-1 cells (Figure 7G–I). RAD51 overexpression did not reduce ER stress in *Eif5* knockdown GC-1 cells (Figure 7G), while rapamycin partially decreased ER-stress-related proteins ATF4 and GRP78, suggesting that

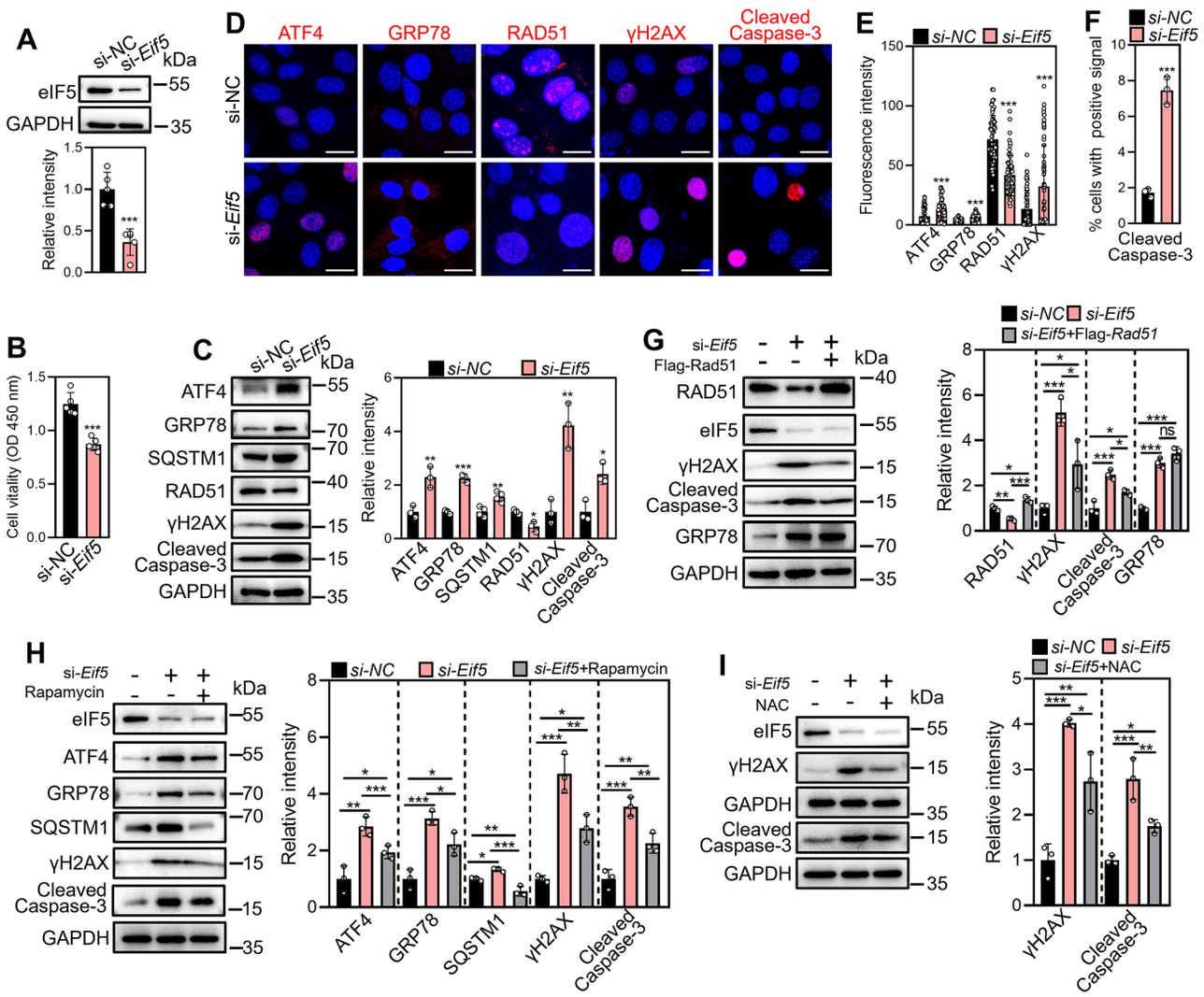

Figure 7 *Eif5* knockdown-induced DNA damage and apoptosis are partially rescued by RAD51 overexpression, rapamycin, and NAC treatment in GC-1 cells

A: Western blot analysis of eIF5 protein levels in GC-1 cells transfected with si-NC or si-*Eif5* for 48 h. GAPDH was used as an internal control. B: CCK-8 assay in GC-1 cells transfected with si-NC or si-*Eif5* for 48 h. C: Western blot analysis of ATF4, GRP78, SQSTM1, RAD51, γH2AX, and Cleaved Caspase-3 protein levels in GC-1 cells. D: Immunofluorescence stainingfor ATF4, GRP78, RAD51, γH2AX, and Cleaved Caspase-3 (red) in GC-1 cells transfected with si-NC or si-*Eif5* for 48 h. Scale bars: 20 μm. E: Quantification of ATF4, GRP78, RAD51, and γH2AX fluorescence intensity in GC-1 cells in D. F: Percentage of Cleaved Caspase-3-positive signal cells in D. G: Western blot analysis of RAD51, eIF5, γH2AX, GRP78, and Cleaved Caspase-3 protein levels in *Eif5* knockdown GC-1 cells following RAD51 overexpression for 48 h. H: Western blot analysis of eIF5, ATF4, GRP78, SQSTM1, γH2AX, and Cleaved Caspase-3 protein levels in *Eif5* knockdown GC-1 cells treated with rapamycin for 48 h. I: Western blot analysis of eIF5, γH2AX, and Cleaved Caspase-3 protein levels in *Eif5* knockdown GC-1 cells treated with NAC for 48 h. For A–C and G–I, n=3–5 independent experiments. For E, more than 300 cells from three independent experiments were analyzed in each group, with every five cells averaged as one data point. For F, more than 300 cells from three independent experiments were analyzed in each group. For G–I, P-values were determined by one-way ANOVA followed by Tukey's test. ns: Not significant; *: P<0.05; **: P<0.01; ***: P<0.001.

restoration of autophagy alleviates ER stress in *Eif5* knockdown GC-1 cells (Figure 7H). These results indicate that impaired DNA repair and elevated ER stress contribute to DNA damage, ultimately leading to apoptosis in *Eif5*-deficient spermatogonia, whereas restoration of autophagy directly attenuates ER stress.

Excessive ER stress and defective DNA repair promote DNA damage and apoptosis in GC-1 cells

To further elucidate the relationship between ER stress and impaired DNA repair in spermatogonia, TG and IBR2 were used to induce ER stress and DNA repair deficiency, respectively, in GC-1 cells. TG treatment reduced fluorescence intensity of AURKB and RAD51, decreased the proportion of EdU^+ cells, and reduced viability in GC-1 cells (Figure 8A–D). In contrast, TG treatment increased fluorescence intensity of ATF4, GRP78, 8-OHdG, and γH2AX, increased the proportion of Cleaved Caspase-3^+ and histone H3 pSer10^+ cells, and elevated ROS levels (Figure 8A–C, E). Consistent with these observations, TG treatment reduced protein levels of RPA2, RAD51, ACO1, BCL-2, and SOD1, while increasing protein levels of ATF4, GRP78, PUMA, γH2AX, and Cleaved Caspase-3 (Figure 8F). In addition, H_2O_2 treatment increased protein levels and fluorescence intensity of γH2AX in GC-1 cells, indicating that elevated ROS levels induce DNA damage (Supplementary Figure S12A, B). IBR2 treatment reduced fluorescence intensity of AURKB, decreased the proportion of EdU^+ cells, and reduced cell viability in GC-1 cells (Figure 8G–J). In contrast, IBR2 treatment increased fluorescence intensity of γH2AX and increased the proportion of histone H3 pSer10^+ and Cleaved Caspase-3^+ cells (Figure 8G–I). Consistent with these results, IBR2 treatment increased protein levels of γH2AX, histone H3 pSer10, and Cleaved Caspase-3 (Figure 8K). However, IBR2 treatment did not alter the levels of ER stress-related proteins, antioxidant-related proteins, or ROS levels (Figure 8K; Supplementary Figure S12C). These findings indicate that elevated ROS generated during excessive ER stress promote DNA damage and apoptosis, and these effects are further exacerbated when DNA repair capacity is impaired in spermatogonia.

DISCUSSION

Mutations affecting components of the translation initiation machinery have been increasingly linked to reproductive abnormalities. The present study revealed that eIF5 was preferentially expressed in male mouse germ cells, including spermatogonia and spermatocytes, compared with somatic cells such as Leydig and Sertoli cells. Conditional deletion of *Eif5* in male germ cells through crossing *Eif5*$^{flox/flox}$ mice with *Stra8*-Cre mice resulted in a marked reduction in SOX3^+ progenitor spermatogonia and KIT$^+$ differentiating spermatogonia, which subsequently led to severe meiotic defects and male infertility. The observed phenotypes are consistent with a model in which elevated ER stress and impaired DNA repair in SOX3^+ progenitor spermatogonia represent central pathogenic mechanisms (Figure 9).

Loss of *Eif5* in male germ cells reduced translation of genes associated with ubiquitination, including *Ddb2, Rnf216*, and *Rad18*, and genes associated with autophagy, including *Atg4b*, *Hmgb1*, and *Smg1*, and this was accompanied by increased ER stress, DNA damage, and apoptosis. Protein ubiquitination plays a critical role in the maintenance of cellular homeostasis via regulation of protein turnover and degradation (Cheng et al., 2021; Umer et al., 2022). Reduced ubiquitination activity may therefore lead to the accumulation of misfolded or damaged proteins, thereby promoting ER stress in SOX3^+ progenitor spermatogonia (Habel et al., 2021; Kandel et al., 2024; Kechko et al., 2019; Li et al., 2022a; Wang et al., 2022). Autophagy supports cell survival through degradation of protein aggregates and damaged organelles (Choi et al., 2020; Seok et al., 2021). Impaired autophagic activity may impede clearance of damaged proteins and organelles, further exacerbating ER stress (He et al., 2019; Maciel et al., 2018; Yeom et al., 2020; Zhang et al., 2022a). Collectively, these findings suggest that ER stress following *Eif5* deletion may result from reduced ubiquitination activity and impaired autophagy, leading to the accumulation of damaged proteins and organelles in SOX3^+ progenitor spermatogonia. In addition, ER stress induced by *Eif5* deletion increased ROS levels, which promoted DNA damage and ultimately apoptosis in SOX3^+ progenitor spermatogonia, consistent with previous reports (Bhattarai et al., 2021; Ma et al., 2022; Zhang et al., 2023, 2022e). Reduced levels of antioxidant-related proteins following *Eif5* deletion may further contribute to elevated ROS levels in SOX3^+ progenitor spermatogonia (Lei et al., 2020a; Madhu et al., 2021).

DNA repair is essential for maintenance of genome stability, regulation of cell cycle progression, and preservation of cell survival, all of which are critical for spermatogonial proliferation and differentiation (Tang et al., 2020; Zhao et al., 2022). In this study, *Eif5* deletion reduced translation of DNA repair-associated genes, including *Rad51* and *Rpa2*, resulting in decreased protein abundance, accompanied by increased DNA damage, cell cycle arrest, and apoptosis in SOX3^+ progenitor spermatogonia. Reduced abundance of DNA repair proteins likely weakens DNA repair function, exacerbating DNA damage (Haase et al., 2022; Wu et al., 2021), which subsequently triggers cell cycle arrest and induces apoptosis (Gomes et al., 2020; Guo et al., 2019; Kaina, 2003). These findings indicate that *Eif5* deletion decreases DNA repair protein abundance and impairs DNA repair capacity, thereby promoting DNA damage and ultimately apoptosis in SOX3^+ progenitor spermatogonia.

Although *Eif5* deletion in male germ cells was initiated at P3, the consequent reduction in germ cell number was not observed until P10 (Lei et al., 2020b). Continued germ cell development in the testes of cKO mice during early stages may be related to reduced ubiquitination activity. Slower degradation may allow residual eIF5 protein to continue supporting translation initiation, while reduced degradation of other proteins may temporarily sustain proliferation and differentiation of SOX3^+ progenitor spermatogonia in the testes of cKO mice. eIF5 functions as a general translation initiation factor; however, deletion of *Eif5* in SOX3^+ progenitor spermatogonia results in a pronounced decrease in the translation of genes associated with ubiquitination, autophagy, and DNA repair. This pattern suggests that proteins involved in these pathways are particularly sensitive to reduced translation initiation activity and are critical for spermatogonial survival. In iNOA patients, insufficient eIF5 activity may therefore contribute to spermatogenic failure through reduced abundance of these key regulatory proteins.

Furthermore, *Eif5* deletion produced distinct cellular outcomes depending on cell type and cell cycle context. Deletion of *Eif5* in oocytes undergoing meiosis and in SOX3+

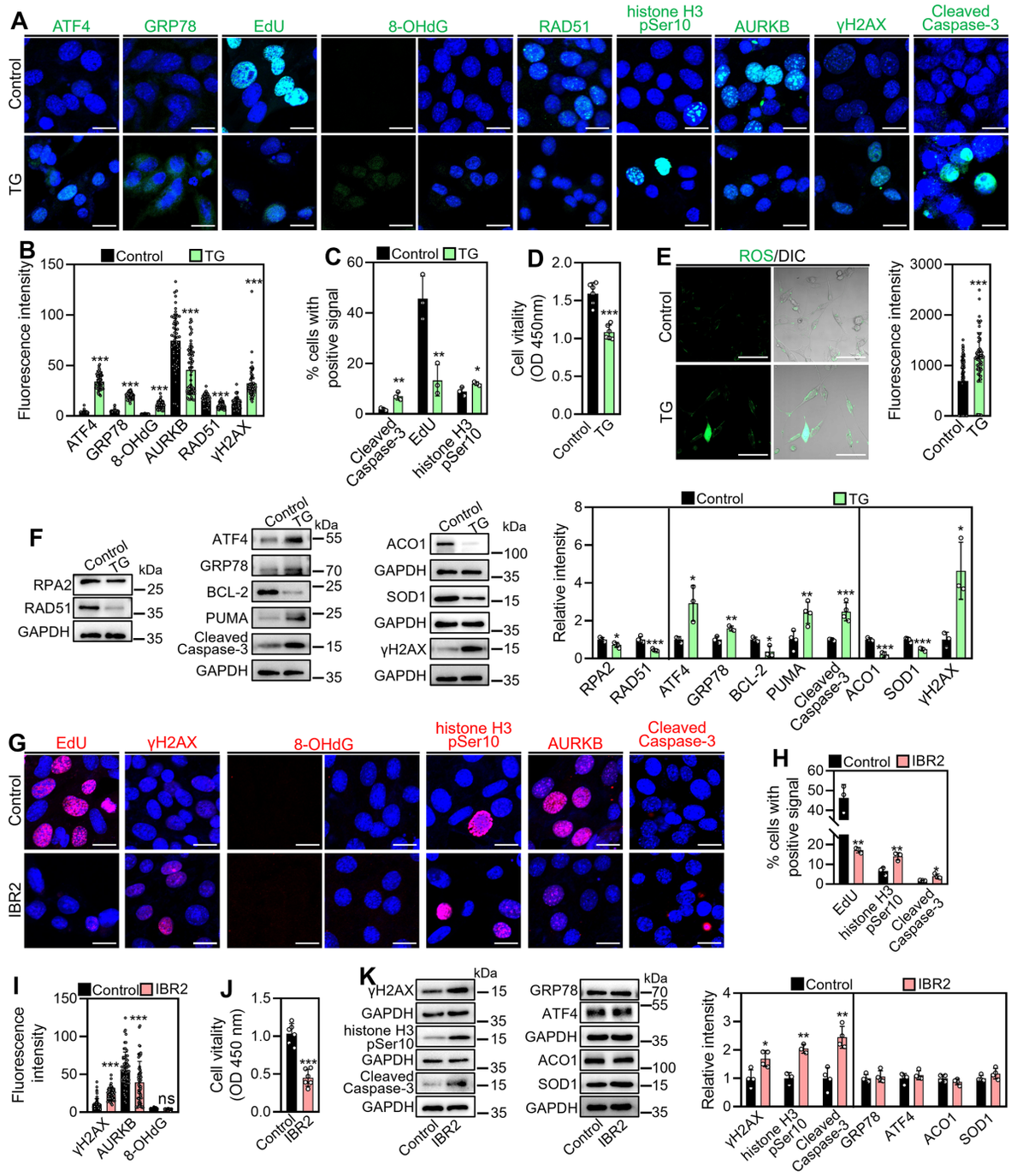

Figure 8 Excessive ER stress and defective DNA repair induce apoptosis in GC-1 cells

A: Immunofluorescence staining for ATF4, GRP78, 8-OHdG, RAD51, histone H3 pSer10, AURKB, γH2AX, and Cleaved Caspase-3, together with EdU (green) incorporation assay, in GC-1 cells after treatment with 0.025 μmol/L TG (endoplasmic reticulum stress inducer) for 48 h. B: Quantification of ATF4, GRP78, 8-OHdG, AURKB, RAD51, and γH2AX fluorescence intensity in GC-1 cells in A. C: Percentage of Cleaved Caspase-3-, EdU-, and histone H3 pSer10-positive cells in A. D: CCK-8 assay in GC-1 cells after treatment with 0.025 μmol/L TG for 48 h. E: Fluorescence staining for ROS using DCFH-DA (green) in GC-1 cells after treatment with 0.025 μmol/L TG for 48 h. F: Western blot analysis of RPA2, RAD51, ATF4, GRP78, BCL-2, PUMA, Cleaved Caspase-3, ACO1, SOD1, and γH2AX protein levels in GC-1 cells after treatment with 0.025 μmol/L TG for 48 h. GAPDH was used as an internal control. G: Immunofluorescence staining for γH2AX, 8-OHdG, histone H3 pSer10, AURKB, and Cleaved Caspase-3, together with EdU (red) incorporation assay, in GC-1 cells after treatment with 10 μmol/L IBR2 (specific RAD51 inhibitor) for 48 h. H: Percentage of EdU-, histone H3 pSer10-, and Cleaved Caspase-3-positive cells in G. I: Quantification of γH2AX, AURKB, and 8-OHdG fluorescence intensity in GC-1 cells in G. J: CCK-8 assay in GC-1 cells after treatment with 10 μmol/L IBR2 for 48 h. K: Western blot analysis of γH2AX, histone H3 pSer10, Cleaved Caspase-3, GRP78, ATF4, ACO1, and SOD1 protein levels in GC-1 cells after treatment with 10 μmol/L IBR2 for 48 h. For B, E, and I, more than 300 cells from three independent experiments were analyzed in each group, with every five cells averaged as one data point. For C and H, more than 300 cells from three independent experiments were analyzed in each group. For D and J, n=6 independent experiments. For F and K, n=3–4 independent experiments. Scale bars: A and G, 20 μm; E, 100 μm. ns: Not significant; *: P<0.05; **: P<0.01; ***: P<0.001.

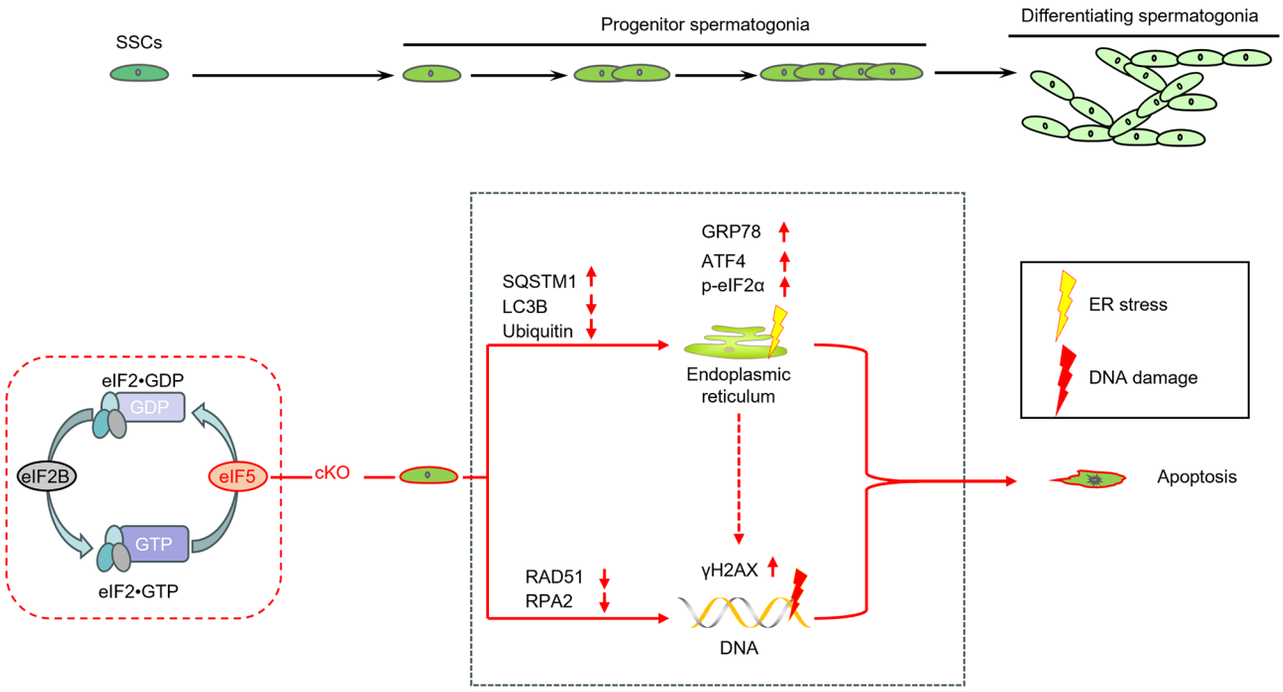

Figure 9 Schematic model of eIF5 function in translation initiation and spermatogenesis

Proliferation and differentiation of SOX3$^+$ progenitor spermatogonia depend on high levels of protein synthesis, a process supported by eIF5 through regulation of translation initiation. During translation initiation, eIF5 promotes hydrolysis of eIF2·GTP to eIF2·GDP and facilitates release of the inactive eIF2·GDP complex. For subsequent rounds of translation initiation, eIF2B converts inactive eIF2·GDP into active eIF2·GTP. Deletion of *Eif5* in male germ cells induces excessive ER stress and impairs DNA repair, leading to apoptosis in SOX3$^+$ progenitor spermatogonia. SSCs, spermatogonial stem cells. Image material was downloaded from ScienceSlides (http://www.scienceslides.com).

progenitor spermatogonia undergoing mitosis both resulted in DNA damage and apoptosis, but through different signaling pathways (Wang et al., 2024). In meiotic oocytes, *Eif5* deletion triggered DNA damage and apoptosis through mitochondrial dysfunction, whereas in mitotic SOX3$^+$ progenitor spermatogonia, *Eif5* deletion induced DNA damage and apoptosis through excessive ER stress and defective DNA repair. In addition, *Eif5* deletion in the testes did not affect *Plzf* mRNA levels but significantly reduced PLZF protein abundance, indicating that regulation occurred at the translational level. Deletion of *Eif5* driven by *Stra8*-Cre affected SOX3$^+$ progenitor spermatogonia but not GFRα1$^+$ stem-like cells. This difference may reflect minimal *Stra8* expression and persistence of eIF5 in GFRα1$^+$ stem-like spermatogonia, in contrast to its absence in SOX3$^+$ progenitor spermatogonia in cKO mice.

Recent research reported abnormal expression of multiple *EIF* genes in the spermatogonia of 13 iNOA patients, with *EIF5* expression shown to be up-regulated in six patients and down-regulated in seven patients. Furthermore, spermatogenesis was arrested at the spermatocyte stage and no sperm were detected in the epididymides of anypatient (Chen et al., 2023). Notably, however, spermatogonial number was reduced in patients with decreased *EIF5* expression but increased in patients with elevated *EIF5* expression. As a GDP dissociation inhibitor, eIF5 also stabilizes binding between eIF2 and GDP (Adomavicius et al., 2019; Keefe et al., 2020). Increased eIF5 expression disrupts formation of the eIF2·GTP complex, thereby inhibiting translation initiation, which may explain iNOA associated with *EIF5* up-regulation. Comparative analysis of differentially expressed transcripts in cKO mouse testes and human spermatogonia with low *EIF5* expression identified 17 overlapping down-regulated transcripts associated with chromosomal stability (*Adad1*, *Dll3*, and *Syce3*), morphogenesis and motility (*Ccdc54*, *Spa17*, and *Spata3*), proliferation and differentiation (*Apitd, Dkkl1*, and *Prr3*), cell cycle regulation (*Cdkn3*, *Cenpu*, and *Oip5*), energy metabolism (*Dpm1*, *Cox17*, and *Gapdhs*), and protein ubiquitination (*Htatip2* and *Ube2t*). These transcripts may contribute to the spermatogenesis defects observed in iNOA.

Overall, *Eif5* deletion promotes apoptosis in SOX3$^+$ progenitor spermatogonia through increased ER stress and decreased DNA repair capacity. These findings offer valuable insights into the pathogenesis of male infertility associated with defective translation initiation factors and may contribute to improved genetic diagnosis and identification of potential therapeutic targets.

DATA AVAILABILITY

The RNA-seq and Ribo-seq data generated in this study have been deposited in the Genome Sequence Archive (GSA) (https://ngdc.cncb.ac.cn/gsa/) under CRA033613, Science Data Bank (https://www.scidb.cn/c/zoores) under DOI: 10.57760/sciencedb.j00139.00309, and NCBI database (https://www.ncbi.nlm.nih.gov/geo/) under accession numbers GSE290783 and GSE290869.

SUPPLEMENTARY DATA

Supplementary data to this article can be found online.

COMPETING INTERESTS

The authors declare that they have no competing interests

AUTHORS' CONTRIBUTIONS

Z.W., M.Z., and H.W. conceived the overall experimental plan. H.W. performed the experiments, analyzed the data, generated the figures, and drafted the manuscript. H.W. conducted bioinformatics analysis. Y.H., H.C., and W.L. contributed to the identification of mouse genotypes and isolation

of mouse testes. W.W., Y.L.S., and S.L. provided advice on *in vivo* studies and participated in partial fluorescence staining and western blot experiments. Y.D., Y.W., L.Z., H.L., and W.Z. participated in the extraction of mRNA and proteins and western blot experiments. Z.W. and M.Z. supervised the research and edited the manuscript. All authors read and approved the final version of the manuscript.

ACKNOWLEDGMENTS

We thank all members of the Meijia Zhang Lab (Innovation Centre of Ministry of Education for Development and Diseases, School of Medicine, South China University of Technology) for their meaningful discussions and guidance. We also thank ScienceSlides (http://www.scienceslides.com) for illustrative components.

REFERENCES

Adomavicius T, Guaita M, Zhou Y, et al. 2019. The structural basis of translational control by eIF2 phosphorylation. *Nature Communications*, **10**(1): 2136.

Anderson MZ, Thomson GJ, Hirakawa MP, et al. 2019. A 'parameiosis' drives depolyploidization and homologous recombination in *Candida albicans*. *Nature Communications*, **10**(1): 4388.

Bai XL, Yang XY, Jia X, et al. 2020. CAV1-CAVIN1-LC3B-mediated autophagy regulates high glucose-stimulated LDL transcytosis. *Autophagy*, **16**(6): 1111–1129.

Berzal-Herranz A, Berzal-Herranz B, Ramos-Lorente SE, et al. 2022. The genomic 3' UTR of flaviviruses is a translation initiation enhancer. *International Journal of Molecular Sciences*, **23**(15): 8604.

Bhattarai KR, Riaz TA, Kim HR, et al. 2021. The aftermath of the interplay between the endoplasmic reticulum stress response and redox signaling. *Experimental & Molecular Medicine*, **53**(2): 151–167.

Chen YD, Liu XX, Zhang L, et al. 2023. Deciphering the molecular characteristics of human idiopathic nonobstructive azoospermia from the perspective of germ cells. *Advanced Science*, **10**(17): 2206852.

Cheng AF, Tse KH, Chow HM, et al. 2021. ATM loss disrupts the autophagy-lysosomal pathway. *Autophagy*, **17**(8): 1998–2010.

Choi I, Zhang YX, Seegobin SP, et al. 2020. Microglia clear neuron-released α-synuclein via selective autophagy and prevent neurodegeneration. *Nature Communications*, **11**(1): 1386.

Chu XG, Subramani K, Thomas B, et al. 2022. Juvenile plasma factors improve organ function and survival following injury by promoting antioxidant response. *Aging and Disease*, **13**(2): 568–582.

Cocetta V, Cadau J, Saponaro M, et al. 2021. Further assessment of *Salvia haenkei* as an innovative strategy to counteract skin photo-aging and restore the barrier integrity. *Aging*, **13**(1): 89–103.

Da Ines O, Bazile J, Gallego ME, et al. 2022. DMC1 attenuates RAD51-mediated recombination in Arabidopsis. *Public Library of Science Genetics*, **18**(8): e1010322.

Di Persio S, Tekath T, Siebert-Kuss LM, et al. 2021. Single-cell RNA-seq unravels alterations of the human spermatogonial stem cell compartment in patients with impaired spermatogenesis. *Cell Reports Medicine*, **2**(9): 100395.

Duan Y, Veksler-Lublinsky I, Ambros V. 2022. Critical contribution of 3' non-seed base pairing to the *in vivo* function of the evolutionarily conserved *let-7a* microRNA. *Cell Reports*, **39**(4): 110745.

Eliseev B, Yeramala L, Leitner A, et al. 2018. Structure of a human cap-dependent 48S translation pre-initiation complex. *Nucleic Acids Research*, **46**(5): 2678–2689.

Feng SL, Li JM, Wen H, et al. 2022. hnRNPH1 recruits PTBP2 and SRSF3 to modulate alternative splicing in germ cells. *Nature Communications*, **13**(1): 3588.

Gomes AL, Matos-Rodrigues GE, Frappart PO, et al. 2020. RINT1 loss impairs retinogenesis through TRP53-mediated apoptosis. *Frontiers in Cell and Developmental Biology*, **8**: 711.

Guo Z, Tian YX, Guo YL, et al. 2019. RAD6B plays a Critical role in neuronal DNA damage response to resist neurodegeneration. *Frontiers in Cellular Neuroscience*, **13**: 392.

Haase S, Banerjee K, Mujeeb AA, et al. 2022. H3.3-G34 mutations impair DNA repair and promote cGAS/STING-mediated immune responses in pediatric high-grade glioma models. *The Journal of Clinical Investigation*, **132**(22): e154229.

Habel N, El-Hachem N, Soysouvanh F, et al. 2021. FBXO32 links ubiquitination to epigenetic reprograming of melanoma cells. *Cell Death & Differentiation*, **28**(6): 1837–1848.

He S, Zeng D, Xu FK, et al. 2019. Baseline serum levels of beclin-1, but not inflammatory factors, may predict antidepressant treatment response in Chinese Han patients with MDD: a preliminary study. *Frontiers in Psychiatry*, **10**: 378.

Huang Q, Liu YH, Zhang SY, et al. 2021. Autophagy core protein ATG5 is required for elongating spermatid development, sperm individualization and normal fertility in male mice. *Autophagy*, **17**(7): 1753–1767.

Kaina B. 2003. DNA damage-triggered apoptosis: critical role of DNA repair, double-strand breaks, cell proliferation and signaling. *Biochemical Pharmacology*, **66**(8): 1547–1554.

Kandel R, Jung J, Neal S. 2024. Proteotoxic stress and the ubiquitin proteasome system. *Seminars in Cell & Developmental Biology*, **156**: 107–120.

Kechko OI, Petrushanko IY, Brower CS, et al. 2019. Beta-amyloid induces apoptosis of neuronal cells by inhibition of the Arg/N-end rule pathway proteolytic activity. *Aging*, **11**(16): 6134–6152.

Keefe MD, Soderholm HE, Shih HY, et al. 2020. Vanishing white matter disease expression of truncated EIF2B5 activates induced stress response. *eLife*, **9**: e56319.

Ki BS, Shim SH, Park C, et al. 2022. Epigenetic regulator Cfp1 safeguards male meiotic progression by regulating meiotic gene expression. *Experimental & Molecular Medicine*, **54**(8): 1098–1108.

Lei KC, Xia YY, Wang XC, et al. 2020a. C/EBPβ mediates NQO1 and GSTP1 anti-oxidative reductases expression in glioblastoma, promoting brain tumor proliferation. *Redox Biology*, **34**: 101578.

Lei WL, Han F, Hu MW, et al. 2020b. Protein phosphatase 6 is a key factor regulating spermatogenesis. *Cell Death & Differentiation*, **27**(6): 1952–1964.

Li N, Zhou QY, Yi Z, et al. 2023. Ubiquitin protein E3 ligase ASB9 suppresses proliferation and promotes apoptosis in human spermatogonial stem cell line by inducing HIF1AN degradation. *Biological Research*, **56**(1): 4.

Li YK, Shen Y, Xie MY, et al. 2022a. LncRNAs *LCETRL3* and *LCETRL4* at chromosome 4q12 diminish EGFR-TKIs efficiency in NSCLC through stabilizing TDP43 and EIF2S1. *Signal Transduction and Targeted Therapy*, **7**(1): 30.

Li ZM, Zhang XZ, Xie SM, et al. 2022c. H3K36me2 methyltransferase NSD2 orchestrates epigenetic reprogramming during spermatogenesis. *Nucleic Acids Research*, **50**(12): 6786–6800.

Li ZR, Wu YH, Fu YB, et al. 2022b. Cyst stem cell lineage eIF5 non-autonomously prevents testicular germ cell tumor formation via eIF1A/eIF2γ-mediated pre-initiation complex. *Stem Cell Research & Therapy*, **13**(1): 351.

Liu WB, Lu XK, Zhao ZH, et al. 2022. SRSF10 is essential for progenitor spermatogonia expansion by regulating alternative splicing. *eLife*, **11**: e78211.

Lu CY, Zhang D, Zhang JL, et al. 2022. Casein kinase 1α regulates murine spermatogenesis via p53-Sox3 signaling. *Development*, **149**(13): dev200205.

Ma J, Dong S, Lu HT, et al. 2022. The hydrogen storage nanomaterial

MgH2 improves irradiation-induced male fertility impairment by suppressing oxidative stress. *Biomaterials Research*, **26**(1): 20.

Maciel M, Hernández-Barrientos D, Herrera I, et al. 2018. Impaired autophagic activity and ATG4B deficiency are associated with increased endoplasmic reticulum stress-induced lung injury. *Aging*, **10**(8): 2098–2112.

Madhu LN, Kodali M, Attaluri S, et al. 2021. Melatonin improves brain function in a model of chronic Gulf War Illness with modulation of oxidative stress, NLRP3 inflammasomes, and BDNF-ERK-CREB pathway in the hippocampus. *Redox Biology*, **43**: 101973.

Mazzitelli JA, Smyth LCD, Cross KA, et al. 2022. Cerebrospinal fluid regulates skull bone marrow niches via direct access through dural channels. *Nature Neuroscience*, **25**(5): 555–560.

Qin JC, Huang T, Wang J, et al. 2022. RAD51 is essential for spermatogenesis and male fertility in mice. *Cell Death Discovery*, **8**(1): 118.

Saewu A, Kongmanas K, Raghupathy R, et al. 2020. Primary Sertoli cell cultures from adult mice have different properties compared with those derived from 20-day-old animals. *Endocrinology*, **161**(1): bqz020.

Seok JK, Hong EH, Yang G, et al. 2021. Oxidized phospholipids in tumor microenvironment stimulate tumor metastasis via regulation of autophagy. *Cells*, **10**(3): 558.

Shu XE, Mao YH, Jia LF, et al. 2022. Dynamic eIF3a *O*-GlcNAcylation controls translation reinitiation during nutrient stress. *Nature Chemical Biology*, **18**(2): 134–141.

Singh CR, Glineburg MR, Moore C, et al. 2021. Human oncoprotein 5MP suppresses general and repeat-associated non-AUG translation via eIF3 by a common mechanism. *Cell Reports*, **36**(2): 109376.

Su R, Dong L, Li YC, et al. 2022. METTL16 exerts an m^6A-independent function to facilitate translation and tumorigenesis. *Nature Cell Biology*, **24**(2): 205–216.

Tang MF, Feng X, Pei GS, et al. 2020. FOXK1 participates in DNA damage response by controlling 53BP1 function. *Cell Reports*, **32**(6): 108018.

Thirouard L, Holota H, Monrose M, et al. 2022. Identification of a crosstalk among TGR5, GLIS2, and TP53 signaling pathways in the control of undifferentiated germ cell homeostasis and chemoresistance. *Advanced Science*, **9**(17): 2200626.

Umer N, Phadke S, Shakeri F, et al. 2022. PFN4 is required for manchette development and acrosome biogenesis during mouse spermiogenesis. *Development*, **149**(16): dev200499.

Vedanayagam J, Lin CJ, Lai EC. 2021. Rapid evolutionary dynamics of an expanding family of meiotic drive factors and their hpRNA suppressors. *Nature Ecology & Evolution*, **5**(12): 1613–1623.

Wang H, Jia XZ, Sui CJ, et al. 2014. Effects of thapsigargin on the proliferation and survival of human rheumatoid arthritis synovial cells. *The Scientific World Journal*, **2014**: 605416.

Wang LH, Arras J, Katsha A, et al. 2017. Cisplatin-resistant cancer cells are sensitive to Aurora kinase A inhibition by alisertib. *Molecular Oncology*, **11**(8): 981–995.

Wang WY, Liu HY, Liu S, et al. 2024. Oocyte-specific deletion of eukaryotic translation initiation factor 5 causes apoptosis of mouse oocytes within the early-growing follicles by mitochondrial fission defect-reactive oxygen species-DNA damage. *Clinical and Translational Medicine*, **14**(8): e1791.

Wang Y, Gao WY, Wang LL, et al. 2022. FBXW24 controls female meiotic prophase progression by regulating SYCP3 ubiquitination. *Clinical and Translational Medicine*, **12**(7): e891.

Wang ZP, Xu XJ, Li JL, et al. 2019. Sertoli cell-only phenotype and scRNA-seq define PRAMEF12 as a factor essential for spermatogenesis in mice. *Nature Communications*, **10**(1): 5196.

Wu C, Peng S, Pilié PG, et al. 2021. PARP and CDK4/6 inhibitor combination therapy induces apoptosis and suppresses neuroendocrine differentiation in prostate cancer. *Molecular Cancer Therapeutics*, **20**(9): 1680–1691.

Xu J, Lu HD, Li HX, et al. 2021. Computerized spermatogenesis staging (CSS) of mouse testis sections via quantitative histomorphological analysis. *Medical Image Analysis*, **70**: 101835.

Yang Y, Fan XJ, Mao MW, et al. 2017. Extensive translation of circular RNAs driven by N^6-methyladenosine. *Cell Research*, **27**(5): 626–641.

Yeom J, Ma S, Lim YH. 2020. Oxyresveratrol induces autophagy via the ER stress signaling pathway, and oxyresveratrol-induced autophagy stimulates MUC2 synthesis in human goblet cells. *Antioxidants*, **9**(3): 214.

Yin HQ, Kang ZL, Zhang YW, et al. 2021. HDAC3 controls male fertility through enzyme-independent transcriptional regulation at the meiotic exit of spermatogenesis. *Nucleic Acids Research*, **49**(9): 5106–5123.

Young-Baird SK, Lourenço MB, Elder MK, et al. 2020. Suppression of MEHMO syndrome mutation in eIF2 by small molecule ISRIB. *Molecular Cell*, **77**(4): 875–886. e7.

Young-Baird SK, Shin BS, Dever TE. 2019. MEHMO syndrome mutation *EIF2S3-I259M* impairs initiator Met-$tRNA_i^{Met}$ binding to eukaryotic translation initiation factor eIF2. *Nucleic Acids Research*, **47**(2): 855–867.

Yuan FF, Wang ZJ, Sun YL, et al. 2021. *Sgpl1* deletion elevates S1P levels, contributing to NPR2 inactivity and p21 expression that block germ cell development. *Cell Death & Disease*, **12**(6): 574.

Zhang C, Wang H, Yang XH, et al. 2022b. Oral zero-valent-molybdenum nanodots for inflammatory bowel disease therapy. *Science Advances*, **8**(37): eabp9882.

Zhang CY, Tan XH, Yang HH, et al. 2022a. COX-2/sEH dual inhibitor alleviates hepatocyte senescence in NAFLD mice by restoring autophagy through Sirt1/PI3K/AKT/mTOR. *International Journal of Molecular Sciences*, **23**(15): 8267.

Zhang J, Pi SB, Zhang N, et al. 2022c. Translation regulatory factor BZW1 regulates preimplantation embryo development and compaction by restricting global non-AUG Initiation. *Nature Communications*, **13**(1): 6621.

Zhang X, Liu BQ, Lal K, et al. 2023. Antioxidant system and endoplasmic reticulum stress in cataracts. *Cellular and Molecular Neurobiology*, **43**(8): 4041–4058.

Zhang XG, Wang LB, Ma YY, et al. 2022d. CEP128 is involved in spermatogenesis in humans and mice. *Nature Communications*, **13**(1): 1395.

Zhang Y, Xu Y, Lu WY, et al. 2022e. G6PD-mediated increase in de novo $NADP^+$ biosynthesis promotes antioxidant defense and tumor metastasis. *Science Advances*, **8**(29): eabo0404.

Zhao S, Hong Y, Liang YY, et al. 2022. Compartmentalized regulation of NAD^+ by Di (2-ethyl-hexyl) phthalate induces DNA damage in placental trophoblast. *Redox Biology*, **55**: 102414.

Zhu JW, Chen HY, Guo XE, et al. 2015. Synthesis, molecular modeling, and biological evaluation of novel RAD51 inhibitors. *European Journal of Medicinal Chemistry*, **96**: 196–208.